2

Climate Forcing, Climate Sensitivity, and Climate Response: A Radiative Modeling Perspective on Atmospheric Aerosols

A.A. LACIS and M.I. MISHCHENKO
Goddard Institute for Space Studies, 2880 Broadway, New York, New York 10025, U.S.A.

ABSTRACT

Atmospheric aerosols are a significant source of direct and indirect global climate forcing. There is a natural aerosol component consisting mostly of soil dust, sea salt, biogenic sulfates, and organic matter that is geographically and seasonally variable; it plays a fundamental role in cloud formation processes, and also makes a small-amplitude direct radiative forcing contribution. There is an anthropogenic component that is linked to fossil-fuel and biomass burning, as well as other human activity; it has been steadily increasing with global industrialization and has been implicated as being responsible for at least partially masking the greenhouse warming due to past greenhouse-gas increases. Major volcanic eruptions such as Pinatubo, which occur infrequently and presumably at random, inject large amounts of sulfuric compounds into the stratosphere, producing a globally dispersed aerosol that reduces the solar energy input and cools the global climate for a period of several years. Such a major volcano can serve as a very effective natural climate forcing experiment to test and calibrate our remote-sensing measurement techniques and capabilities, and to assess the ability of our global climate models to predict the magnitude and duration of the climate perturbation in response to the radiative forcing imposed by the volcanic aerosol.

INTRODUCTION

Climate forcing is thought primarily to be radiative in nature whereby a small sustained *change* in either solar or thermal radiation is *imposed* on the planet's radiation energy balance, driving the climate system to a new thermal equilibrium. Atmospheric aerosols exert both a *direct* and an *indirect* forcing on climate: the former, by

Aerosol Forcing of Climate
Edited by R.J. Charlson and J. Heintzenberg

interacting directly with the solar and thermal radiation fields; the latter, by affecting either the amount or the radiative properties of other components of the climate system, and thus indirectly producing additional radiative forcing.

From a modeling perspective, direct radiative forcing by aerosols can be accurately calculated, at least in principle, once the optical constants, size distribution, and atmospheric concentration of the aerosol are known. The difficult part is predicting and modeling the time evolution of the climate system's response in reaction to the imposed forcing. This is because changes in temperature caused directly by the imposed radiative forcing produce feedback reactions within the climate system that tend to magnify and geographically shift the direct effect of the forcing.

Positive feedback appears to dominate in the terrestrial climate (e.g., in response to a forcing perturbation that causes warming, the resulting increase in atmospheric water vapor and melting of snow/ice generates additional radiative forcing which produces a further increase in climate warming). Also, the feedbacks are latitude dependent, with the polar regions exhibiting greater climate sensitivity, i.e., a more strongly positive feedback. Furthermore, the time evolution of the climate response to external forcing is strongly moderated by the large heat capacity of the ocean and by atmosphere–ocean interactions. But perhaps the greatest impediment to being able to predict the climate response to applied radiative forcing accurately is the indeterministic nature of the terrestrial climate system (Lorenz 1968), which produces unforced "natural" variability even in the absence of external forcing.

Typical atmospheric aerosols of concern are of the order of 1 μm in radius or less and are mostly nonabsorbing at visible wavelengths. Hence, the expected impact on climate is cooling of the global surface temperature because of reduced solar heating due to radiation being scattered back to space. More realistic aerosol treatment considers also the absorption of sunlight by aerosols (which, for soot, and possibly desert dust, is sufficiently large to cause warming of the global climate). Radiative modeling of aerosols should also incorporate the absorption and emission at thermal wavelengths that contribute a small, but not negligible, addition to the atmospheric greenhouse effect.

Accurate determination of the indirect aerosol effect is more problematic since this involves complex physical interactions that are not fully understood. For example, heterogenous chemistry on aerosol surfaces plays an important role in the formation of the Antarctic ozone hole (Toon and Turco 1991) and in the catastrophic loss of stratospheric ozone (Prather 1992) at low and middle latitudes after the Pinatubo volcanic eruption (see Toon, this volume). In a technical sense, clouds might be considered as being entirely a product of indirect aerosol forcing, since cloud condensation, as we know it, would not take place in a truly aerosol-free atmosphere (e.g., Andreae 1995). Rather, by indirect aerosol cloud forcing we mean the relative effect that *enhanced* cloud condensation nuclei (CCN) concentrations, particularly in industrialized and polluted areas, have on cloud microphysical processes, leading to increased cloud albedo and longevity (Twomey et al. 1984; Charlson et al. 1992), over and above their "natural" unperturbed levels (see Blanchet, this volume).

The global mean radiative forcing contributed by greenhouse gas (GHG) increases over the past century (2.0 W m^{-2} to 2.5 W m^{-2}) has been well documented (e.g., Hansen and Lacis 1990). However, despite the greatly improved understanding of aerosols and aerosol processes, the radiative forcing attributable to aerosol changes over the past century, which are quite likely to have significantly masked the GHG forcing, is still available only as a semiquantitative estimate. Part of the reason for this is the greater radiative complexity of aerosols, their large variability geographically and with time, and their relatively short atmospheric lifetime. However, in addition to these modeling related problems, the persistent uncertainty in aerosol forcing is compounded by the continued absence of a global satellite monitoring system that is capable of measuring and monitoring changes in aerosol amounts and their radiative properties with sufficient accuracy.

MODELING NEEDS

Given that the atmospheric distribution of aerosols were either adequately observed or prescribed, in order to determine the aerosols' radiative impact on climate, we need:

- the optical constants (complex refractive index) at all wavelengths of interest for the chemical compounds contained in aerosols;
- the chemical composition, particle shape, and size distribution of aerosol species;
- a suitable Mie-scattering model to compute the aerosol radiative parameters (Q_x, ω_0, and $\beta(\phi)$, i.e., the extinction efficiency, single-scattering albedo, and phase function, respectively, with ϕ being the scattering angle) for all wavelengths of interest;
- a suitable radiative transfer model to calculate the absorption and scattering effects of aerosols in the context of a realistic atmosphere;
- a physical model to determine the effect of hygroscopic particle growth with changing relative humidity on the optical and radiative parameters of hygroscopic aerosols;
- a cloud microphysical model to determine changes in cloud particle size, optical depth, and longevity in response to changes in CCN concentration;
- a chemistry model to determine the impact on atmospheric ozone distribution due to heterogeneous chemistry on aerosol surfaces;
- a comprehensive general circulation model (GCM) with interactive ocean for realistic simulation of the transient climate response.

Optical Parameters

We need first to know the chemical composition of the aerosol, along with its real and imaginary refractive index components over the full range of visible and thermal

wavelengths. The basic information is generally available, at least for the principal chemical constituents of atmospheric aerosols (e.g., WMO 1983). However, as pointed out long ago by Toon et al. (1976), there are both fundamental and practical problems in obtaining reliable optical constants and radiative parameters for a given atmospheric aerosol.

For example, while optical constants can be readily measured in the laboratory for pure chemical compounds that are known to be constituents of atmospheric aerosols, it is not correct to average the optical constants to simulate the complicated mix of chemical compounds and impurities that characterize typical aerosols. This is because the radiative properties of scattering particles are not linear functions of the optical constants and must also be cross-section weighted to obtain the radiative parameters for use in radiative transfer calculations. Thus, even if we were to make a direct laboratory determination of the radiative parameters of a given aerosol sample, the results would be "sample specific" and not be directly applicable to aerosols with a different mix of impurities, or for the same composition but with a different distribution of particle sizes. There is a related problem in being able to model the effect on aerosol refractive indices and radiative parameters caused by the change in composition and particle radius for hygroscopic particles as they respond to changes in relative humidity (Hänel 1976).

In view of the obvious complexity of aerosol composition, there is a clear need for improving and expanding the current database of aerosol optical constants. Moreover, the potential pitfalls in using aerosol radiative parameters calculated directly from the available optical constants are sufficiently real to make it absolutely necessary to perform appropriate *in situ* validation measurements of aerosol radiative properties in order to obtain closure (see Ogren, this volume).

Radiative Parameter Model

Whether the available refractive index database is adequate or not is a question that needs to be seriously evaluated. Nevertheless, given the optical constants, the radiative parameters that fully describe the radiative properties of the aerosol can then be rigorously calculated using Mie-scattering theory for homogeneous particles that are spherical in shape (e.g., Hansen and Travis 1974). These radiative parameters are the normalized extinction efficiency, Q_x^n, the single-scattering albedo, ω_0, and the phase function, $\beta(\phi)$, which can often be approximated with reasonable accuracy by the asymmetry parameter, g. (Here, Q_x^n is the extinction efficiency factor, Q_x, normalized to unity at $\lambda = 0.55$ μm, where in turn, Q_x is the average extinction cross-section divided by the average particle geometric cross-sectional area).

Since radiative transfer modeling of the direct forcing cares only about the aerosol optical depth, and not specifically about the particle number density, it is convenient to normalize the extinction efficiency factor at a reference wavelength ($\lambda = 0.55$ μm), and to use the extinction optical depth, δ, at this wavelength as the measure of aerosol column amount (with a vertical profile to specify the atmospheric distribution with

height). The optical depth at this reference wavelength can be related to the aerosol number density through the value of Q_x at $\lambda = 0.55$ μm, values of which are given in Table 2.1 for the particle sizes and compositions illustrated below.

The refractive index information that we used for input to the Mie-scattering calculations is taken from Palmer and Williams (1975) for concentrated H_2SO_4, Toon et al. (1976) for ammonium sulfate, Nilsson (1979) for soot and sea salt, and Patterson et al. (1977) and Volz (1973) for desert dust, respectively.

The spectral dependence on particle size of the aerosol radiative parameters (Q_x^n, ω_0, and g) is illustrated in Plate 2.1a (lefthand panels) for a concentrated sulfuric acid composition (75% H_2SO_4 by weight) characteristic of stratospheric aerosols. The particle size distributions shown, calculated for the standard gamma size distribution (see below), range from effective radius $r_e = 0.1$–1.0 μm, with effective variance $v_e = 0.2$, and are characteristic of the size modes observed for the El Chichon volcanic aerosol (Hofmann and Rosen 1983). The spectral range from 0.3–30 μm serves to cover the principal contributing regions of the solar and thermal spectra, with 3 μm roughly separating the solar and thermal regimes. Also included for comparison in Plate 2.1a (and in Table 2.1) are the results for the log normal size distribution ($r_o = 0.05$, $\sigma_g = 2$) that was used by Kiehl and Briegleb (1993) to represent sulfate aerosol forcing (with H_2SO_4 refractive index spectral dependence). Referenced by its effective radius $r_e = 0.166$ μm, with effective variance $v_e = 0.693$ compared to $v_e = 0.2$ for the gamma distribution results, the log normal distribution is depicted by the yellow lines in Plate 2.1a.

For thermal radiation, the smaller particles tend to be more absorptive (smaller ω_0) because for these sizes and wavelengths the particles are situated in the Rayleigh regime. Also, there is a steady shift with wavelength that signals the onset of the "small particle regime," where the asymmetry parameter g begins its steady decrease to zero with increasing wavelength. Note, however, that the thermal efficiency factors do not decrease monotonically with particle size (when normalized to unit efficiency at $\lambda = 0.55$ μm). This apparent increase in thermal extinction for $r_e = 0.1$ μm relative to larger sizes is caused by the relatively greater rate of extinction decrease that occurs at visible wavelengths for these small particle sizes (see Table 2.1). This happens because these particles are in the size parameter range that falls on the steepest part of the resonance slope of the scattering efficiency curve (Hansen and Travis 1974).

Table 2.1 Extinction efficiency factors at $\lambda = 0.55$ μm.

H_2SO_4	Q_x	$r_e = 0.5$ μm	Q_x
$r_e = 1.0$	2.522	Desert Dust	2.931
$r_e = 0.5$	3.014	Sulfate	2.969
$r_e = 0.3$	2.716	Sea Salt	3.016
$r_e = 0.1$	0.409	Soot	2.523
$r_e = 0.166$	1.162	2 μm Dust	2.280

Plate 2.1a illustrates the progressive shift in the radiative parameter spectral dependence as the effective radius r_e changes. Radiative parameters of the log normal distribution (yellow lines, r_e = 0.166 μm) are bounded by the r_e = 0.1 μm and r_e = 0.3 μm curves for wavelengths less than ~ 2 μm, or when the particle size parameter is of order unity or greater. Since the log normal distribution variance is significantly broader than the gamma distribution variance, there are more large particles in the large particle tail of the log normal distribution. This difference is amplified at long wavelengths, where the bulk of the particles in the size distribution fall within the "small particle regime" with much reduced scattering contributions. In these circumstances, contributions from the large particle tail of the distribution tend to dominate, such that at thermal wavelengths, Q_x and g of the log normal distribution (r_e = 0.166 μm) exceed the gamma distribution values for r_e = 0.3 μm.

In Plate 2.1b (righthand panels), the spectral dependence of the radiative parameters is illustrated for different compositions (desert dust, sulfate, sea salt, and soot) for particles having the same gamma size distribution with r_e = 0.5 μm and v_e = 0.2. Basically, the results show that, except for soot, the radiative parameter dependence on composition, though significant, is not nearly as great as the parameter dependence on particle size. A strong spectral dependence on particle size, such as that shown in Plate 2.1a for sulfuric acid, is implicit for each of the composition curves in Plate 2.1b. To further underscore this point, we include in Plate 2.1b the radiative parameters calculated for a larger size mode of desert dust with effective radius r_e = 2 μm and v_e = 0.2 (the yellow curves labeled Dust 2). This strong spectral dependence on particle size carries over both solar and thermal wavelength regimes, and underscores the need for accurate determination of not only the effective radius, but also the effective variance of aerosol size distributions.

Most notable is the strong increase in absorption at visible wavelengths for the larger-sized dust particles and the strong increase in extinction at thermal wavelengths. The increased absorption in the visible results from the lengthened path for refracted light traveling through the particles. For wavelengths greater than about 2.5 μm, however, the dust particles are in the size parameter regime where ω_0 increases with particle size. This nonlinear dependence of the radiative parameters on particle size serves to demonstrate the complex behavior of aerosol radiative parameters and the need to determine accurately both the composition and size distribution of atmospheric aerosols.

While naturally occurring aerosols span a continuum in particle size, shape, and composition that is variable geographically, and also with height and time, radiative modeling considerations permit only a finite number of aerosol sizes and compositions to be carried in the calculations. Thus, for example, the H_2SO_4 aerosol in the stratosphere may be multimodal with an effective radius that corresponds to none of those shown in Plate 2.1a. The approach that we adopt here to resolve this problem is to assume that the radiative parameters of the actual size distribution of the aerosol can be obtained either by interpolating or by taking a weighted average from within the available base sizes that are carried in the model.

Particle Size Distribution

To eliminate the spurious high-frequency ripple in radiative parameter values that occurs in monodisperse size distributions due to single particle interference effects (e.g., Hansen and Travis 1974), some reasonable dispersion in aerosol sizes is needed. The results in Plate 2.1 were calculated using the gamma size distribution with a moderately broad effective variance of $v_e = 0.2$, for selected values of effective radius r_e. Given the strong dependence of aerosol radiative parameters on particle size, there is indeed a problem in being able to specify accurately the aerosol size distribution when aerosols come in such a wide range of particle sizes spanning several orders of magnitude. The size spectrum of desert dust, for example, undergoes tremendous variations in particle concentration depending on prevailing weather conditions (d'Almeida 1987; Duce, this volume). The practical problem is how best to describe a given aerosol size distribution in terms of a few parameters that can be simply related to the radiative properties of the aerosol.

Many different analytical forms for size distributions have been described in the literature. WMO (1983) suggests using a three-term log normal distribution, where each term represents a different mode radius. Hansen and Travis (1974) show that the radiative properties of an aerosol are not particularly sensitive to the specific analytic form of the size distribution that is used (see also Mishchenko and Travis 1994b). Rather, the one key parameter that best describes the radiative properties of a given size distribution is the cross-section weighted effective radius r_e, which is defined as:

$$r_e = G^{-1} \int_0^\infty r\, \pi r^2\, n(r)\, dr\,, \tag{2.1}$$

where $n(r)dr$ is the fraction of particles with radii from r to $r + dr$, such that the integral over $n(r)$ is unity. The corresponding effective variance is defined as:

$$v_e = (G r_e^2)^{-1} \int_0^\infty (r - r_e)^2\, \pi r^2\, n(r)\, dr\,, \tag{2.2}$$

where

$$G = \int_0^\infty \pi r^2\, n(r)\, dr \tag{2.3}$$

is the average particle geometric cross-sectional area. For our purposes, the standard gamma distribution

$$n(r) = C\, r^{(1 - 3b)/b}\, e^{-r/(ab)} \tag{2.4}$$

is very convenient for dealing with size distributions since the distribution parameters a and b are also equal to the effective radius, r_e, and to the effective variance, v_e, respectively. Hence, for the gamma distribution, we see that changing the variance of the size distribution does not alter the effective radius, as it does in other size distributions. The normalization constant, C, is equal to $(ab)^{(2b-1)/b}/\Gamma[(1-2b)/b]$. Different moments of the gamma size distribution are given by

$$\overline{r^n} = \int_0^\infty r^n \, n(r) \, dr \,, \tag{2.5}$$

yielding

$$\overline{r^n} = (ab)^n \, \frac{\Gamma[(1-2b)/b + n]}{\Gamma\,[(1-2b)/b]} \,, \tag{2.6}$$

or,

$$\overline{r^n} = a^n \prod_{k=1}^{n} \, [1 + (n-k-2)b] \,. \tag{2.7}$$

For the gamma distribution, the column mass loading per unit area of the aerosol M is related to the reference optical depth δ at $\lambda = 0.55$ μm and the column number density of particles per unit area through

$$M = \frac{4}{3} \pi a^3 \, (1-b) \, (1-2b) \, \rho \, H N \tag{2.8}$$

and

$$\delta = \pi a^2 \, (1-b) \, (1-2b) \, Q_x \, H N \,, \tag{2.9}$$

where a and b are the effective radius and variance, respectively, ρ is the specific density of the aerosol, Q_x is the extinction efficiency factor at $\lambda = 0.55$ μm, H is the column height, and N is the total number of particles per unit volume. The quantity $\pi a^2(1-b)(1-2b)$ is also equal to G, the average geometric cross-sectional area of particles. The column mass loading of aerosol is thus defined in terms of the effective radius, specific density, and the optical depth and extinction efficiency factor at the reference wavelength $\lambda = 0.55$ μm by

$$M = \frac{4}{3} \, r_e \, \rho \, \delta \, Q_x^{-1} \,, \tag{2.10}$$

a relationship that is more generally applicable to other size distributions as well, in particular to the log normal distribution as described below.

The log normal distribution, which is frequently used in describing aerosol size distributions, is given by

$$n(r) = (2\pi)^{-1/2} (\sigma_0 r)^{-1} \exp\left[\frac{-(lnr - lnr_0)^2}{2\sigma_0^2}\right], \tag{2.11}$$

where r_0 is the geometric mean radius, and where $\sigma_0 = ln(\sigma_g)$, the natural logarithm of σ_g, the geometric standard deviation. In terms of log normal parameters, the effective radius is given by

$$r_e = r_0 \exp\left[\frac{5}{2}\sigma_0^2\right], \tag{2.12}$$

and effective variance by

$$v_e = \exp\left[\sigma_0^2\right] - 1\,. \tag{2.13}$$

The different moments of the log normal distribution are given by

$$\overline{r^n} = r_0^n \exp\left[\frac{n^2\sigma_0^2}{2}\right]. \tag{2.14}$$

Accordingly, the column mass loading per unit area and the optical depth at the reference wavelength are, for the log normal distribution, given by

$$M = \frac{4}{3}\pi r_0^3 \exp\left[\frac{9}{2}\sigma_0^2\right] \rho H N\,, \tag{2.15}$$

and

$$\delta = \pi r_0^2 \exp\left[2\sigma_0^2\right] Q_x H N\,, \tag{2.16}$$

respectively.

In reporting aerosol size distributions, it is important to remember that for radiative transfer purposes, the key parameter is the area-weighted effective radius, which can either be calculated directly from numerically binned size distribution data or derived from any convenient analytic size distribution. However, the maximum variance for which the gamma distribution is defined is $v_e = 0.5$, which corresponds to $\sigma_0 = 0.636$, or $\sigma_g = 1.89$, for the log normal distribution. A practical problem arises in using very broad log normal distributions when calculating radiative parameters, since such a

distribution can exhibit a physically unrealistic dependence on "phantom" 10–100 μm size particles that are implicitly contained within the large particle tail of the size distribution. This happens when σ_g becomes significantly greater than ~3. Thus, it is preferable to describe aerosol size distributions as consisting of several moderately broad-sized modes that are physically significant or distinct, each with their individual size distribution parameters, rather than attempt to fit the entire aerosol size spectrum with a single very broad-sized distribution (see also Raes et al., this volume). This is also consistent with current understanding of chemical composition as a function of size, and with respect to dynamics.

Nonspherical Particles

For nonspherical aerosols, an efficient method has recently been developed to calculate rigorously light scattering by size-shape distributions of randomly oriented axially symmetric particles (Mishchenko 1993). Detailed theoretical comparisons of the radiative properties of nonspherical polydispersions and Mie-scattering results (Mishchenko and Travis 1994a, b) show that nonspherical particle effects can be large and important in remote-sensing applications, i.e., where it is necessary to invert measurements of bi-directional intensities, or of linear polarization, in order to retrieve aerosol optical depth and size information. Even though climate modeling applications require knowledge only of the radiative fluxes and albedos, essentially all retrieval methods of aerosol radiative properties utilize intensity measurements. Accordingly, this poses a potentially serious interpretation problem for nonspherical aerosols such as windblown desert dust. By utilizing the polarimetric signature of aerosols in addition to intensity, a significant improvement in retrieval reliability can be achieved for aerosol radiative parameters.

Plate 2.2 shows the degree of linear polarization for aerosols as a function of phase angle (defined as 180°-scattering angle) and effective size parameter $x_e = 2\pi r_e / \lambda$ for polydispersions of volume-equivalent spheroids (Plate 2.2a) and spheres (Plate 2.2b) calculated with the index of refraction $1.5 + 0.02i$ similar to that of tropospheric dust aerosols. The aspect ratio (i.e., the ratio of the largest to smallest particle dimensions) of the spheroids is 1.7, which is a typical value measured by Nakajima et al. (1989) for yellow desert dust particles. It is seen that particle nonsphericity can change not only the magnitude of polarization but even its sign.

In Plate 2.3, the ratio (nonspherical phase function/spherical phase function) is displayed as a function of phase angle for the same set of particles displayed in Plate 2.2. Plate 2.3 shows that, depending on particle size parameter, the ratio of nonspherical to spherical intensities can be as large as 3 at sidescattering angles, and as small as 0.4 at backscattering angles. This strongly suggests that nonspherical/spherical differences in the scattered intensity must be explicitly taken into account when interpreting bi-directional reflectance measurements, e.g., from satellites (see also Koepke and Hess 1988).

The unequivocal interpretation of measured radiances in terms of volume-equivalent spheres can lead to large errors in retrieved aerosol optical depth if the aerosols turn out to be nonspherical. Indeed, using a model for spherical particles to invert bi-directional measurements of nonspherical aerosols over a dark surface (e.g., ocean) can greatly overestimate the retrieved aerosol optical depth for measurements taken at side-scattering angles, while for backscattering angles the optical depth would be greatly underestimated. A retrieval model that utilizes polarimetric measurements acquired over sufficient phase angle range can readily differentiate between spherical and nonspherical aerosols, and thus provide a more complete physical description of aerosol properties.

On the other hand, for climate modeling applications, where only radiative flux and albedo information are required, Mie-scattering calculations made for equivalent volume spheres appear to give adequate accuracy, provided that the optical depth, size distribution, and refractive index of the aerosol are known *a priori*. This is illustrated in Plate 2.4, and summarized in Table 2.2, for a simple model composed of an aerosol layer of optical depth $\delta = 0.1$ situated above a Lambertian surface with albedo A_L.

Table 2.2 Radiative properties of polydisperse, randomly oriented spheroidal desert dust aerosols vs. volume-equivalent spheres. The aspect ratio for nonspherical aerosols is 1.7 (Nakajima et al. 1989). Dust refractive index is $1.53 + 0.01i$; effective variance is 0.2.

Size Parameter x_e =	5	10	15	20	25	30
g (spheroids)	0.702	0.711	0.740	0.787	0.820	0.843
g (spheres)	0.693	0.720	0.766	0.823	0.846	0.859
ω_0 (spheroids)	0.923	0.849	0.782	0.744	0.715	0.690
ω_0 (spheres)	0.920	0.846	0.781	0.752	0.720	0.693
Global Albedo ($A_L = 0$)						
Spheroids	0.031	0.025	0.020	0.016	0.013	0.011
Spheres	0.031	0.025	0.019	0.015	0.012	0.011
HG (spheroids)[1]	0.031	0.027	0.023	0.018	0.015	0.013
HG (spheres)[1]	0.032	0.026	0.021	0.016	0.012	0.012
Global Albedo ($A_L = 0.6$)						
Spheroids	0.587	0.570	0.555	0.546	0.540	0.536
Spheres	0.587	0.569	0.554	0.548	0.541	0.536
HG (spheroids)[1]	0.587	0.570	0.555	0.546	0.540	0.535
HG (spheres)[1]	0.587	0.569	0.555	0.548	0.541	0.535

[1]Calculations for Henyey-Greenstein (HG) phase function use an asymmetry parameter and single-scattering albedo equal to that of the respective spheroidal or spherical aerosol.

Given the large differences in phase function between the spheroidal phase function and the equivalent sphere Mie-scattering phase function as shown in Plate 2.3, the very close agreement in the calculated plane albedos is rather surprising. In fact, the common approximation of using the Henyey-Greenstein phase function (for the respective asymmetry parameters and single-scattering albedos) produces considerably larger errors in solar zenith angle dependence than the nonspherical–spherical difference. Typically, the Henyey-Greenstein approximation underestimates aerosol backscatter (at high sun angles) and overestimates sidescattering (at low sun angles); however, the integral over sun angle (spherical albedo) shows remarkably good agreement with the more rigorous phase function treatment (Table 2.2). Nonspherical–spherical differences in the global (spherical) albedo are diluted by increasing surface albedo and are small enough to be considered insignificant. Despite great nonspherical–spherical differences in the angular distribution of the scattered intensity (Plate 2.3), angular integration makes the differences in the plane and global albedos essentially negligible.

Composite Radiative Parameters

In radiative transfer modeling of aerosols, it is numerically convenient and practical to represent the aerosol as consisting of a weighted average of discrete size distributions and chemical species, such as those shown in Plate 2.1. Each of the characteristic aerosol size modes and compositions is then described by its individual vertical profile and column optical depth referenced at a reference wavelength ($\lambda = 0.55$ μm); the spectral dependence of its radiative parameters is obtained from the Mie-scattering results that are presented as a function of wavelength in Plate 2.1.

Given the above, we can then tabulate the radiative parameters Q_x, ω_0, and g for realistic aerosol compositions and size distributions. The radiative parameters (as functions of wavelength) of the composite aerosol are obtained by summing up the individual monochromatic extinction optical depths

$$\delta_x = \delta_{x,1} + \delta_{x,2} + \delta_{x,3} + \ldots . \tag{2.17}$$

The approach is completely general, assuming only that a given aerosol can be approximated by means of a weighted average taken over a set of reference size and/or composition species. The corresponding composite-scattering optical depth is similarly obtained as

$$\delta_{sc} = \delta_{sc,1} + \delta_{sc,2} + \delta_{sc,3} + \ldots , \tag{2.18}$$

where $\delta_{sc,i} = \omega_{0,i}\delta_{x,i}$ is the scattering optical depth of the i^{th} component. The single-scattering albedo for the composite aerosol is obtained as the ratio of total scattering optical depth to total extinction optical depth, i.e., $\omega_0 = \delta_{sc}/\delta_x$. The composite asymmetry

parameter is obtained then as the weighted average with respect to individual scattering optical depths

$$g = (g_1\delta_{sc,1} + g_2\delta_{sc,2} + g_3\delta_{sc,3} + \ldots)/\delta_{sc} \,. \tag{2.19}$$

The above recipe is repeated at each wavelength for all layers of the atmosphere that contain aerosols. Contributions to the total extinction and scattering optical depths by clouds and gaseous absorbers that overlap the aerosol can be included in analogous fashion. The resulting sets of composite parameter values δ, ω_0, and g then become the basic input parameters to the radiative transfer model. In this fashion, the radiative parameters of different aerosol size modes and/or compositions can be combined for radiative modeling. For a more precise treatment of the multiple scattering angle dependence, we should use the full phase function $\beta(\phi)$ in place of the asymmetry parameter g.

Radiative Transfer Model

Because of the strong solar zenith angle dependence of multiple scattering for small optical depths (e.g., Plate 2.4a), accurate results require the use of fairly rigorous and numerically expensive computational methods such as the doubling and adding method. For typical two-stream methods commonly used in climate modeling applications, King and Harshvardhan (1986) show that albedo errors of 10%–20% are commonplace in single-layer calculations. Also, these errors tend to increase for absorbing aerosols and may be further aggravated in a multilayered atmosphere. Although integration over sun angle averages out much of this error, a residual bias with latitude is likely to remain. Accordingly, the radiative modeling of aerosols in climate models presents some challenges in parameterization.

To compute radiative properties of aerosols, we use a multiple scattering parameterization based on the doubling/adding method (Lacis and Hansen 1974) that is also being used in the GISS GCM (Hansen et al. 1983). This radiative model is designed to reproduce the doubling/adding solar zenith angle dependence for conservative scattering. To determine the spectral dependence of aerosol radiative properties, we apply the radiative model monochromatically to the radiative parameters in Plate 2.1 for an aerosol optical depth of $\delta = 0.1$ (at reference wavelength $\lambda = 0.55$ μm), and surface albedo $A_L = 0$. The results of these multiple scattering calculations are then integrated over solar zenith angle to obtain the spherical (global) spectral reflectivity (albedo), transmission, and absorption, which are plotted in Plate 2.5 for the same particle size modes of H_2SO_4 and the selected compositions (desert dust, sulfate, sea salt, and soot) as displayed in Plate 2.1.

The upper panels in Plate 2.5 show the monochromatic global albedo as a function of wavelength across both solar and thermal wavelengths. (The nonzero reflectivity that remains prominent at thermal wavelengths suggests that multiple scattering might not be entirely negligible in the thermal, particularly for H_2SO_4 and desert dust). Direct

and diffuse transmissions are combined and shown in the middle panels. At solar wavelengths, sulfate, sea salt, and H_2SO_4 are essentially nonabsorbing, hence the spectral dependence of the total transmission mirrors that of reflection. (This is because the albedo, total transmission, and absorption must sum to unity at each wavelength to conserve energy). Soot, on the other hand, is a powerful absorber at all wavelengths, but it still reflects some of the incident radiation. Desert dust, depending on particle size, can also absorb a substantial amount of solar radiation. Sulfuric acid, desert dust, soot, and also sulfate show significant absorption at thermal wavelengths (bottom panels), particularly in the 10 μm window region, indicating that these aerosols can contribute significantly to the atmospheric greenhouse, particularly for the larger particle sizes.

Smaller values of the asymmetry parameter are associated with the smallest size particles (e.g., $r_e = 0.1$ μm H_2SO_4) and thus tend to enhance scattering to compensate partially for the smaller extinction cross-sections. However, most of the wavelength dependent differences exhibited in the radiative parameters (Plate 2.1), and their dependence on particle size and composition are retained in the spectral dependence of the albedo, transmission, and absorption. To obtain a measure of the aerosol radiative forcing potential in a form that is suitable for radiative model intercomparisons, the results in Plate 2.5 are weighted by solar spectrum and integrated over the interval 0.3–5.0 μm. Spectrally integrated global albedo and global absorption for sulfuric acid and the other selected compositions are shown in Table 2.3 for $\delta = 0.1$ of aerosol. For reference, the corresponding global incident solar radiation is 332.55 W m^{-2}.

It is rather remarkable that the spectrally integrated global albedos in Table 2.3 are as similar as they are, given the very large differences in spectral extinction particularly as a function of particle size. (For the range of H_2SO_4 particle sizes covered, the global albedo varies only by 10%–15% from the mean value). This may perhaps help to explain the rationale for choosing $\lambda = 0.55$ μm as the reference wavelength for aerosol optical depths, as either a shorter or longer reference wavelength would shift the relative magnitudes of global albedos between the larger and smaller particle size modes. For comparison, the log normal distribution of H_2SO_4 with $r_e = 0.166$ μm fits smoothly among the gamma size distribution numbers. The albedo and absorption for

Table 2.3 Spectrally integrated reflection and absorption for $\delta = 0.1$.

H_2SO_4	R(W m^{-2})	A(W m^{-2})	r_e = 0.5 μm	R(W m^{-2})	A(W m^{-2})
r_e = 1.0	11.02	0.35	Desert Dust	10.39	3.39
r_e = 0.5	9.03	0.15	Sulfate	10.86	0.13
r_e = 0.3	7.78	0.10	Sea Salt	9.34	0.02
r_e = 0.1	11.33	0.19	Soot	3.63	31.18
r_e = 0.166	8.83	0.12	2 μm Dust	8.50	10.08

the 2 μm desert dust particles show substantial reduction in reflectivity and a marked increase in absorptivity relative to $r_e = 0.5$ μm dust particles.

Since the results in Table 2.3 were calculated for an isolated aerosol layer with zero surface albedo and with no other atmospheric components present, these results represent only the upper limit in radiative forcing for $\delta = 0.1$ of aerosols and are thus more useful for intercomparing aerosol radiative properties and their dependence on particle size and composition in simplified circumstances. At $\delta = 0.1$, global albedos are in a radiative regime that is still sensibly linear, i.e., for $\delta = 0.2$, the global albedos need only be discounted by about 10%, and for $\delta = 0.3$, by about 20%.

More realistic estimates for the radiative forcing by aerosols require that the radiative calculations be performed in the context of a global atmosphere that includes overlapping absorption by ozone, water vapor, and CO_2, with surface, cloud, and Rayleigh scattering under clear and cloudy sky conditions. For this purpose we use a radiative model similar to that of the GISS GCM, but with more spectral intervals for both the solar and thermal radiation (36 and 31 intervals, respectively, with each interval subdivided into 10 k-distribution subintervals). A cloud cover of 50% is assumed, with high, middle, and low clouds comprising 10%, 10%, and 30%, respectively, with optical depths of 2, 8, and 16 set to yield a global planetary albedo of about 0.30. Global mean profiles of ozone and water vapor are prescribed, along with climatological values of other atmospheric trace gases. The spectral integration over gaseous absorption and cloud, aerosol, Rayleigh scattering in the visible is by means of k-distributions, whereby absorption coefficients from noncontiguous regions of the spectrum are grouped together according to their absorption strength (Lacis and Oinas 1991).

For thermal wavelengths, we use the nonscattering approximation to compute the radiative fluxes, i.e., the absorption optical depth $\delta_{ab} = \delta_x - \delta_{sc}$, or equivalently, $\delta_{ab} = \delta_x(1 - \omega_0)$ is used, an approach that eliminates explicit dependence on the aerosol phase function or asymmetry parameter. Physically, this approximation assumes that the scattered fraction of incident light is scattered entirely in the forward direction, and thus effectively remains "unscattered," which, for strongly absorbing particles at thermal wavelengths, is not a bad approximation since most of the radiation that is scattered is located within the diffraction peak. Overlapping absorption with gaseous absorbers is handled by means of k-distributions.

Thus defined, the radiative model is run to radiative-convective equilibrium (yielding a global mean surface temperature of about 288 K) and is ready for calculating the radiative forcing and corresponding change in global equilibrium temperature for prescribed changes in aerosol and other climatic perturbations in the context of a realistic global atmosphere.

CLIMATE FORCING

In defining radiative climate forcing, the basic objective is to find a simple measure of radiative flux change in response to a climate perturbation that can be related

accurately to the eventual change in global surface temperature. *Instantaneous forcing* is defined as the change in net flux at the tropopause level of the atmosphere in response to the applied perturbation, calculated for a fixed atmospheric structure. This is a relatively simple calculation that usually provides a good estimate of the eventual equilibrium change in global surface temperature, particularly when the radiative perturbation produces a simple change in planetary albedo or greenhouse efficiency. If, however, the forcing perturbation also produces a significant change in the stratospheric temperature, the flux balance at the tropopause will be altered by rapid readjustment in stratospheric temperature, leading to a biased estimate of the eventual surface temperature change. As an illustrative example, we note that the instantaneous change in net flux at the tropopause caused by ozone changes in the lower stratosphere may differ both in sign and in magnitude from the temperature change that actually takes place (e.g., Rind and Lacis 1993).

A better estimate of the radiative forcing is obtained by allowing the stratospheric temperature to equilibrate before evaluating radiative flux changes (e.g., IPCC 1990). *Adjusted forcing* is obtained by allowing the stratospheric temperature to reach its new radiative equilibrium following the perturbation, while keeping ground and tropospheric temperatures fixed, and by not allowing feedback effects (such as melting of snow, increase in water vapor, or change in clouds) to operate. Differences in solar and thermal fluxes are then taken with respect to the equilibrium flux values of the comparison control run to establish the change in the planetary energy balance at the top of the atmosphere (TOA).

For the aerosol species listed in Table 2.3, we compute both the instantaneous and adjusted radiative forcing for a $\Delta\delta = 0.1$ increase in aerosol optical depth, and present the results in Table 2.4. The H_2SO_4 column in Table 2.4 depicts stratospheric aerosols distributed uniformly between 20 and 25 km; the right-hand columns depict tropospheric aerosols with $r_e = 0.5$ μm located between 0 and 3 km. The sign convention for flux changes is such that negative values of the change in net solar flux, ΔF_{sol}, signify loss in global solar energy input (cooling), and positive values in net thermal flux, ΔF_{thrm}, signify increased greenhouse trapping (warming). Since the solar flux is not sensitive to stratospheric temperature change, the instantaneous radiative forcing is given by the sum $\Delta F_{sol} + \Delta F^{o}_{thrm}$, while the adjusted forcing, following stratospheric equilibration, is given by the sum $\Delta F_{sol} + \Delta F_{thrm}$.

The placement of aerosols in realistic atmospheric context reduces the reflected solar radiation by a factor of 2 to 3 compared to the "upper limit" results in Table 2.3. For absorbing aerosols, such as soot and desert dust, a more complicated interaction with the atmospheric environment is evident, including a significant dependence on particle size and altitude. Overall, the radiative forcing by $\Delta\delta = 0.1$ of aerosol change is comparable to the 4 W m^{-2} forcing for doubled CO_2, but of opposite sign for the nearly conservative scattering aerosols. Results for the log normal H_2SO_4 distribution, with $r_e = 0.166$ μm confined to the bottom 1 km of the atmosphere, as in the Kiehl and Briegleb (1993) calculations with $\Delta\delta = 0.1$, yield –2.70 W m^{-2} global forcing.

Table 2.4 Solar and thermal global radiative forcing[1] (W m^{-2}) for $\Delta\delta = 0.1$ of aerosol.

H_2SO_4	ΔF_{sol}	ΔF_{thrm}	ΔF^{o}_{thrm}	$r_e = 0.5$ μm	ΔF_{sol}	ΔF_{thrm}	ΔF^{o}_{thrm}
$r_e = 1.0$	–5.60	2.19	1.76	Desert Dust	–2.61	0.05	0.08
$r_e = 0.5$	–4.21	0.91	0.69	Sulfate	–3.59	0.06	0.10
$r_e = 0.3$	–3.32	0.62	0.45	Sea Salt	–3.05	–0.03	0.01
$r_e = 0.1$	–4.08	1.20	0.96	Soot	6.62	0.28	0.19
Desert Dust ($r_e = 2$ μm)				0 to 3 km	–0.22	0.47	0.47
				0 to 6 km	0.68	1.33	1.35
H_2SO_4 ($r_e = 0.166$ μm)				0 to 1 km	–2.70	–0.03	0.02

ΔF_{sol} and ΔF_{thrm} are total-sky globally averaged adjusted radiative forcings at TOA. Global mean atmospheric structure with 50% cloud cover is used in a radiative-convective equilibrium model to compute the flux changes. ΔF^{o}_{thrm} is the instantaneous radiative forcing evaluated at the tropopause.

To provide a measure of the aerosol greenhouse contribution, the instantaneous change in thermal flux at the tropopause, ΔF^{o}_{thrm}, is also included in Table 2.4. (ΔF^{o}_{thrm} is also of interest since it is the thermal component of the instantaneous radiative forcing evaluated at the tropopause, a quantity that is widely used and is simpler to obtain than the more accurate adjusted radiative forcing at TOA that is preferentially used in the text). Clearly, the greenhouse contribution by aerosols is important in the stratosphere where its magnitude is seen to increase rapidly with particle size. This strong dependence on particle size is also evident for desert dust aerosols for which the thermal greenhouse forcing increases by a factor of six in going from $r_e = 0.5$ μm to 2 μm. Since the greenhouse forcing is proportional to the temperature contrast between the aerosol local temperature and the ground surface temperature, raising the aerosols to higher altitude will also enhance their greenhouse forcing. Thus, by mixing the aerosols uniformly to a height of 6 km, their greenhouse forcing is increased by nearly a factor of three, as shown by the desert dust example. Still, the greenhouse contribution by submicron tropospheric aerosols appears to be largely insignificant, and, as in the case of sea salt, it is completely overwhelmed by the increment in downwelling thermal radiation from the stratosphere, caused by the small increase in stratospheric temperature due to increased ozone absorption of upwelling solar radiation that is scattered upward by the aerosol.

This small increase in absorption by ozone of the incremental increase in upwelling solar radiation results in a small decrease in ΔF_{sol} between the tropopause and TOA. We ignore this small difference in evaluating the (total) instantaneous aerosol forcing. For adjusted forcing, we use the TOA values of ΔF_{sol} and ΔF_{thrm} since they reflect the actual changes in the planetary radiation budget. Note also that in the case of adjusted forcing, the *total* net flux change remains invariant between the tropopause and TOA.

It is generally recognized that large differences exist in the radiative forcing exerted by aerosols under clear-sky and cloudy-sky conditions. Since our calculations were done for 50% cloud cover, the clear-sky radiative forcing is readily obtained in the form $\Delta F_{clear} = \Delta F_{total} + \Delta D$, where ΔF_{total} represents the total-sky flux differences given in Table 2.4, and ΔD (tabulated in Table 2.5) denotes the respective clear-sky minus cloudy-sky flux differences (divided by two) for the same $\Delta\delta = 0.1$ of aerosol change. Similarly, the cloudy-sky radiative forcing is obtained in the form $\Delta F_{cloudy} = \Delta F_{total} - \Delta D$.

For the nearly conservative scattering aerosols, the ratio of clear-sky to cloudy-sky radiative forcing ranges from about 2.3 for the 1 μm stratospheric aerosols to about 3.5 for tropospheric sulfate and sea salt. This ratio, however, is dramatically affected by aerosol absorptivity, exceeding 13 for the $r_e = 0.5$ μm desert dust for which the single-scattering albedo at visible wavelengths is of order $\omega_0 = 0.95$. Moreover, for the 2 μm desert dust, the radiative forcing changes sign from –2.73 W m^{-2} under clear-sky conditions to +2.29 W m^{-2} under cloudy conditions, with further magnification of the cloudy-sky forcing (to +4.32 W m^{-2}) when the aerosol is mixed to higher altitudes (6 km), where the aerosol can more effectively impact the cloud single-scattering albedo and absorb a part of the upwelling radiation that is reflected by clouds.

Besides affecting the planetary radiation balance, absorbing aerosols, under both clear and cloudy skies, can strongly impact the atmospheric deposition of absorbed solar energy. In the extreme case of soot, the global mean clear-sky atmospheric absorption increases by 25.43 W m^{-2} for $\Delta\delta = 0.1$, while absorption at the ground decreases by 22 W m^{-2}, with an increase in absorbed solar energy at TOA by 3.43 W m^{-2}. Under cloudy skies, the atmospheric absorption by soot remains high (22.47 W m^{-2}) while absorption at the ground decreases by 12.41 W m^{-2}, leaving 10.06 W m^{-2} as the TOA cloudy-sky radiative forcing. Considering that total global mean atmospheric absorption is ~75 W m^{-2}, $\Delta\delta = 0.1$ of soot is clearly a large perturbation of the climate system.

In comparing the thermal flux sums and differences between Tables 2.4 and 2.5, we see that the tropospheric aerosol greenhouse contribution, small as it is, is almost

Table 2.5 Clear-sky – total-sky solar and thermal flux differences for $\Delta\delta = 0.1$ of aerosol.

H_2SO_4	ΔD_{sol}	ΔD_{thrm}	ΔD^o_{thrm}	$r_e = 0.5$ μm	ΔD_{sol}	ΔD_{thrm}	ΔD^o_{thrm}
$r_e = 1.0$	–2.23	0.19	0.02	Desert Dust	–2.25	0.03	0.05
$r_e = 0.5$	–1.78	0.07	0.01	Sulfate	–1.98	0.05	0.08
$r_e = 0.3$	–1.47	0.04	0.01	Sea Salt	–1.69	–0.02	0.00
$r_e = 0.1$	–2.10	0.09	0.01	Soot	–3.44	0.10	0.14
Desert Dust ($r_e = 2$ μm)				0 to 3 km	–2.51	0.31	0.35
				0 to 6 km	–3.65	0.51	0.58
H_2SO_4 ($r_e = 0.166$ μm)				0 to 1 km	–1.37	0.01	0.02

entirely a clear-sky phenomenon. On the other hand, greenhouse forcing by stratospheric aerosols is only 15%–20% stronger under clear-sky conditions compared to cloudy skies, a result of the greater temperature contrast between the ground and stratosphere compared to that of cloud and stratosphere. The nonzero differences in instantaneous flux at the tropopause, ΔD°_{thrm}, for stratospheric aerosols are not greenhouse related, but are due to the equilibrium stratosphere being slightly warmer over cloudy skies than clear skies due to the greater ozone absorption of reflected sunlight.

Aerosol column amounts are often given in terms of mass loading per unit area. This can lead to uncertainties in aerosol forcing, by factors of 2 to 3, if the aerosol size is not known. This potential range in uncertainty is illustrated in Table 2.6 where the total radiative forcing in Table 2.4 has been rescaled by the specific densities representative of the aerosol compositions.

For the nonabsorbing aerosols, this potential uncertainty range is somewhat narrower if the aerosol is known only in terms of its reference optical depth. The peak scattering efficiency, on a per unit mass basis, is achieved for particles that have effective radius near 0.3 μm. There is a much wider range in the potential uncertainty of radiative forcing for the absorbing aerosols. Thus it is abundantly clear that full information on aerosol size, optical depth, and composition is required in order to determine the radiative forcing by aerosols with reasonable accuracy.

The above results identify the key aerosol parameters that are important for determination of aerosol radiative properties and provide the framework for understanding the role of aerosols in the radiative forcing of global mean climate. Aerosols, however, are spatially quite variable and need to be placed in realistic global context such as that provided in GCM simulations. Such maps of global radiative forcing have been computed by Tegen and Lacis (1994) for windblown mineral dust, and by Kiehl and Briegleb (1993) for anthropogenic sulfates (see also Kiehl and Rodhe, this volume).

Tropospheric Aerosols

The major tropospheric aerosol types may be grouped into five basic categories: soil dust, sulfates, sea salt, soot, and organic aerosols. Of these, much attention has been

Table 2.6 Total-sky global radiative forcing (W m^{-2}) per mg m^{-2} of aerosol.

H_2SO_4	ρ (g cm^{-3})	ΔF_{total}	r_e = 0.5 μm	ρ (g cm^{-3})	ΔF_{total}
r_e = 1.0	1.7	–0.038	Desert Dust	2.5	–0.045
r_e = 0.5	1.7	–0.088	Sulfate	1.8	–0.087
r_e = 0.3	1.7	–0.108	Sea Salt	2.0	–0.070
r_e = 0.1	1.7	–0.052	Soot	2.0	0.131
Desert Dust (r_e = 2 μm)			0 to 3 km	2.5	0.009
			0 to 6 km	2.5	0.069
H_2SO_4 (r_e = 0.166 μm)			0 to 1 km	1.7	–0.084

focused on the sulfate aerosol, of which the anthropogenic component has increased dramatically during the past several decades (Charlson et al. 1992). Kiehl and Briegleb (1993) have calculated the globally averaged annual forcing contribution by the sulfate aerosols to be -0.3 W m^{-2}, an amount that could have significantly masked part of the ~ 2 W m^{-2} of greenhouse forcing accumulated over the past century. The sulfate aerosol is the end product in a complex chain of chemical and physical processes that convert natural and anthropogenic emissions of sulfur-bearing compounds into sulfate aerosol (see Möller, this volume). To gain a better understanding of the climate forcing exerted by sulfate aerosols, it is important to relate the current atmospheric sulfate burden to its paleoclimatic context (Legrand, this volume), and thus provide a better baseline for projecting future trends in anthropogenic aerosols (see Hidy and Wolf, this volume).

Windblown soil dust is transported globally by the general circulation of the atmosphere from its major sources in arid and semiarid regions (see Duce, this volume). The size distribution of soil dust varies widely with time and location as dust storms lift particles as large as 100 μm into the atmosphere. The largest particles fall out rapidly, but particles on the order of 1 μm in radius are carried thousands of kilometers from their source regions. As described in the previous sections, the climatic impact of soil dust ranges from definite cooling to definite warming of the surface temperature, depending on the particle size and also on the vertical distribution of the aerosol. Hence, the impact of soil dust on the global energy balance cannot be accurately characterized until a more precise climatology of particle sizes and optical depths is established.

Carbonaceous aerosols constitute a broad category of particulate matter associated with biomass burning, fragments of plant material, and converted emissions of organic and industrial vapors (see Penner, this volume). Since representative refractive indices of organic aerosols are not available from which to calculate radiative parameters and their spectral dependence, the radiative forcing by organic aerosols is quite uncertain. Penner et al. (1992) estimate that smoke aerosol due to biomass burning may contribute as much as -1 W m^{-2} of forcing and may thus be an important anthropogenic contributor. Elemental carbon, which appears as a common strongly absorbing component in organic aerosols, is often separately categorized as "soot." The other components of organic type aerosols remain rather poorly characterized in terms of their radiative properties and thus constitute a major source of uncertainty in our determination of the direct radiative forcing contributed by aerosols.

The indirect climate forcing exerted by the anthropogenic sulfate and biomass burning aerosols is also difficult to quantify and could well exceed the direct forcing in magnitude by altering cloud optical thicknesses and lifetimes. *In situ* measurements of ship tracks and stratocumulus clouds at remote locations confirm an indirect aerosol effect on clouds; however, the validity of extrapolating this relationship globally remains to be ascertained (King et al., this volume). Additional evidence pointing to indirect aerosol forcing of climate is the 0.5°C decrease in diurnal cycle amplitude over large portions of the Earth's land areas during the period 1951–1990, comparable in magnitude to the mean warming of these same regions (Karl et al. 1993; Karl et al.,

this volume). GCM modeling results of diurnal temperature range sensitivity to climate forcing parameters (Hansen *et al.* 1995) suggest that such a large decrease in diurnal amplitude cannot be achieved with continentally located aerosols alone, but requires an increase in continental cloud cover possibly as a consequence of indirect anthropogenic aerosol forcing. The magnitude of the required cloud change to model the observed decrease in diurnal amplitude range is 3%–5% over the affected land areas, not inconsistent with currently available observational constraints.

Stratospheric Aerosols

The ability both to characterize the radiative forcing and to confirm the climate response to this forcing is uniquely available for stratospheric aerosols. This is because (a) nature provided an unprecedented climate experiment in the form of the Pinatubo eruption and (b) adequate satellite and ground-based instrumentation were in place to make the appropriate measurements. The SAGE II measurements, along with the support of numerous ground-based observations, characterized the time evolution of the volcanic aerosol cloud, including its vertical and spatial distribution (McCormick and Veiga 1992). Balloonborne measurements (Deshler et al. 1992) determined the chemical composition to be concentrated H_2SO_4/H_2O solution and also characterized the particle size distribution. Detailed analysis of sunphotometer measurements (Russell et al. 1993) show the effective radius of the volcanic aerosol increasing from $r_e = 0.22$ μm a month following the mid-June, 1991, eruption, to $r_e = 0.56$ μm after two months, and $r_e = 0.86$ μm a year after the eruption. Further confirmation of the particle size is provided by extinction measurements made in the thermal window region (Pollack et al. 1991), which found a volume modal radius of 0.6 μm. Efforts continue to analyze and assimilate all available Pinatubo measurements to define a precise and detailed time dependent climatology of the Pinatubo aerosol.

Based on preliminary estimates of the Pinatubo eruption parameters (global mean peak optical depth $\delta = 0.15$, effective radius $r_e = 0.5$ μm), Hansen et al. (1992) calculated the peak radiative forcing of the volcanic aerosol to be about –4.5 W m^{-2} occurring in early 1992, and, based on the time evolution of the previous large El Chichon eruption, decaying to zero by the end of 1995. This information was input to the GISS GCM to calculate the climate response to the volcanic forcing. A global cooling by about –0.5°C by the end of 1992 was predicted, with recovery to normal by 1995. The GCM also predicted a decrease in tropospheric temperature by –0.5°C and a stratospheric temperature increase by about 2°C, primarily due to the absorption of upwelling thermal radiation by the Pinatubo aerosol. Plate 2.6 (updated from Hansen, Lacis et al. 1993) shows a generally close agreement between the observed and the modeled changes in stratospheric, tropospheric, and global ground surface temperatures, thus providing some measure of closure for the Pinatubo stratospheric aerosol experiment. The magnitude and time dependence of the Pinatubo radiative forcing has also been confirmed in ERBE measurements of the solar and thermal radiative flux changes at TOA (Minnis et al. 1993). In Plate 2.6, stratospheric

temperatures are 30 mb zonal means at 10°S, while the model results are for the 10 to 70 mb stratospheric layer at 8°S to 16°S, the other temperatures being global averages. In the GCM simulation, climatic effects of the near-simultaneous El Niño event were not included. As the Pinatubo aerosol climatology is updated and ancillary climatic data become generally available, more detailed model comparisons will be possible.

The stratosphere has proven to be an ideal setting for conducting climate impact studies of volcanic type aerosols, partly because the volcanic aerosol is dominated by a single chemical species, and also because the stratosphere is relatively isolated from other competing radiative contributors. This makes it possible to illustrate more clearly the dependence of radiative forcing on particle size distribution parameters, including also the aerosol's direct effect on the local stratospheric temperature.

Plate 2.7a shows the change in the solar and thermal radiative forcing components as a function of r_e for a H_2SO_4 aerosol with optical depth of $\delta = 0.1$. As particle size becomes larger than the contributing solar wavelengths, the extinction efficiency Q_x becomes essentially independent of r_e, and the solar flux change approaches an asymptotic value. The thermal (greenhouse) contribution, however, continues to increase with particle size as extinction efficiency increases in the thermal window region of the spectrum, such that for particles larger than $r_e = 2.2$ μm, their greenhouse effect exceeds their albedo effect and causes warming of the global surface temperature, rather than cooling.

Plate 2.7b shows the local stratospheric heating within the 20 to 25 km region occupied by the aerosol, also for an optical depth of $\delta = 0.1$. Heating by solar radiation is seen to increase with r_e due to increased absorption at near-infrared wavelengths as a result of increasing Q_x (see Plates 2.1 and 2.5). Thermal heating, however, reaches its peak efficiency in the vicinity of $r_e = 2$ μm, then declines. This is partly because of saturation effects (as layer temperature increases, emission to space also increases, but at all wavelengths of the spectrum), and also because extinction efficiency, and therefore thermal emission, increases with r_e in the spectral regions beyond 10 μm, from which the layer primarily cools to space. Hence the solar and thermal components of stratospheric heating exhibit saturation effects and do not sum linearly.

For particles in the size range typical of volcanic aerosols ($r_e \sim 0.5$ μm), stratospheric heating is caused almost entirely by the absorption of upwelling thermal radiation by the aerosol. The radiative effects of stratospheric aerosols, given their composition and distribution, are determined primarily by their optical depth δ and effective radius r_e. Dependence on the variance v_e of the aerosol size distribution is weak, though not negligible (Lacis et al. 1992).

Stratospheric temperature measurements (e.g., Labitzke and McCormick 1992) indirectly place useful constraints on the compositional impurities that may be present in the volcanic aerosol. This is because the stratospheric temperature change is strongly dependent on the single-scattering albedo of the aerosol. For example, H_2SO_4 aerosol of optical depth $\delta = 0.1$, but with $\omega_0 = 0.98$ at visible wavelengths, would produce stratospheric temperature increases in excess of 5°C (Lacis et al. 1992), far above what

was actually observed. This implies that the single-scattering albedo of volcanic aerosol must be very close to unity, i.e., no significant impurities that would cause significant absorption can be present, except perhaps locally during the initial phases of the eruption, which was poorly covered by observations.

It is also instructive to place the Pinatubo climate forcing in perspective by noting that the peak forcing of -4.5 W m^{-2} due to the aerosol optical depth of $\delta = 0.15$, *if sustained*, would put the Earth in an ice age climate (Pollack et al. 1993). This illustrates the importance of the very large heat capacity of the ocean in moderating climate change by imposing a very long time scale for radiative forcing to reach equilibrium.

CLIMATE SENSITIVITY

Climate sensitivity is commonly expressed in terms of the global mean equilibrium surface temperature change (degrees K) that would take place (if the climate system were able to reach equilibrium) in response to a specified amount of radiative forcing (W m^{-2}) imposed by a climate perturbation such as doubled CO_2. The climate response to the perturbation is not a simple readjustment in atmospheric temperature that just reimposes global energy balance. Rather, the response involves complex feedback processes that can either magnify or diminish the direct effect of the imposed perturbation.

Adjusted radiative forcing is thought to provide a reasonably good measure for estimating the equilibrium temperature change that will take place in response to an imposed radiative forcing, independent of the perturbation type. It is assumed, thus, that the climate system cares only about the magnitude of the forcing, and not particularly where in the atmosphere the forcing is applied, or whether the forcing affects solar or thermal radiation. The basic validity of these assertions is supported by GCM climate experiments that have been performed for doubled CO_2 and 2% increase in solar constant, which produce nearly the same change in equilibrium temperature response (~ 4 K) for similar (~ 4 W m^{-2}) imposed radiative forcing (Hansen et al. 1984). To first order, greenhouse forcing by CO_2 and increased solar energy input produce very similar global mean climate responses. A further assumption (also largely borne out by GCM climate experiments) is that the different feedback processes are ultimately driven by temperature change. On this basis, it is possible to form a quantitative description of GCM feedback and climate sensitivity, using the results of GCM experiments.

To illustrate this, we use GCM results from a doubled CO_2 experiment that yields 3.85°C for the global annual mean difference in equilibrium surface temperature between the experiment and control runs. To be more generically in tune with the topic of radiative forcing by aerosols, we perhaps should have used a global change in aerosol loading to perform the following feedback analysis. However, we use the doubled CO_2 results in our feedback sensitivity analysis partly to emphasize the point

that feedback sensitivity, to first order, should be independent of the type of applied forcing, and also because CO_2 forcing has been more thoroughly studied in climate change literature.

The equilibrium zonal annual mean (ZAM) temperature differences from this experiment are shown by the solid black line in the top panel of Plate 2.8. If we focus on the annual mean values of the different climate variables and use the annual time period in defining energy input and output from given latitudinal intervals, then clearly the ZAM temperature differences must be definable in terms of ZAM climate variable changes in a local energy balance equilibrium sense, i.e., the changes in atmospheric water vapor, clouds, temperature lapse rate, surface albedo, and advective transports that took place between the experiment and control runs must fully explain the ZAM temperature differences (otherwise the temperatures would not be in equilibrium).

By running the GCM radiation code in a radiative–convective–advective (RCA) equilibrium mode using the ZAM climate variables, we can construct a zonal RCA equilibrium model that can reproduce the global annual mean results of the GCM control and experiment runs. With this model, we can calculate the change in annual mean temperature that is associated with each specific change in water vapor, cloud cover, surface albedo, etc., occurring between the experiment and the control run. In this fashion, we can apportion the total ZAM temperature change among the different radiative contributors shown in Plate 2.8a (top panel). (Actually, the sum of the colored plus the dotted lines only *approximates* the solid black line, indicating that actual feedback interactions are a bit more complicated than described). In any case, in this description, the colored lines represent feedback contributions, while the dotted black line is the forcing term (ΔT_0 in Hansen et al. (1984) terminology, which represents radiative forcing expressed as an equilibrium temperature change, with *no* feedbacks operating). Note that CO_2 forcing expressed in terms of equilibrium temperature change is nearly constant with latitude ($\Delta T_0 \sim 1.2$ K), as opposed to CO_2 forcing expressed as radiative forcing in W m^{-2} (see Kiehl and Rodhe, this volume), which necessarily reflects the Planck function dependence on the zonal temperature.

If we assume that climate feedbacks are ultimately temperature driven, it follows then that the feedback efficiency is obtained simply by dividing the apportioned temperature change for each respective feedback type by the total ZAM temperature change at that latitude. This has the effect of associating all feedback-induced changes in atmospheric water vapor, clouds, melting of snow/ice, etc., with the total change in ZAM temperature. The feedback efficiency factors thus defined are shown in Plate 2.8b (middle panel). Although derived for CO_2 forcing, the characteristic feedback efficiencies are more generally applicable to other types of forcing and, for small changes in forcing, would be expected to remain basically fixed.

Overall, we see that water vapor feedback (includes increase in column amount, vertical redistribution of water vapor, and change in atmospheric lapse rate) is a strong positive feedback at all latitudes, accounting for 0.43 of the total global temperature change. Cloud feedback (includes change in cloud cover and cloud height, but not change in cloud radiative properties) is also positive at low to middle latitudes, but

negative in the polar regions. Globally averaged, cloud feedback accounts for 0.15 of the temperature change. Snow/ice feedback (depends mostly on changes in sea ice) is strongly positive in the polar regions, accounting there for more than 0.5 of temperature change. Globally averaged, snow/ice feedback accounts for 0.11 of the temperature change. Advective feedbacks (include changes in meridional transport of geopotential energy and transport of latent and sensible heat) also have significant latitudinal dependence (with a tendency to counteract cloud feedback at low and middle latitudes), but globally, advective feedbacks average to zero.

The black dotted line in Plate 2.8b is the fractional CO_2 contribution to the total temperature change and therefore has a different meaning than the other (feedback efficiency) curves. Instead, the CO_2 line depicts the fraction of the zonal temperature change *not* due to feedbacks.

The feedback efficiency factors are linearly additive, but the feedback magnification factor (Hansen et al. 1984) that relates equilibrium climate response to the imposed climate forcing is given by

$$\Delta T_{eq} = (1 - f_e)^{-1} \Delta T_{0,} \tag{2.20}$$

where ΔT_{eq} is the global equilibrium temperature change and ΔT_0 is the imposed global mean forcing expressed in temperature units. Temperature forcing, ΔT_0, is related to the radiative forcing, ΔT_0, by a flux conversion factor, i.e., $\Delta T_0 = k_0 \Delta F_0$, where $k_0 = 0.3$ K/W m^{-2} is the (no feedback) global mean flux conversion factor which is obtained as a Planck function weighted average of flux change contributions. Thus, globally averaged,

$$\Delta T_{eq} = k_0(1 - f_e)^{-1} \Delta F_0 \,. \tag{2.21}$$

For the doubled CO_2 experiment, the globally averaged feedback efficiency factors sum to $f_e = 0.69$, implying a feedback magnification factor, $f_m = (1 - f_e)^{-1}$, which multiplies the imposed forcing by a factor of 3.2.

In Plate 2.8c (bottom panel), climate feedback sensitivity is expressed in terms of equilibrium temperature change (degrees K) divided by the adjusted radiative forcing (W m^{-2}) imposed at TOA. The individual feedback sensitivities are indicated by their respective colors. The solid black line depicts the climate sensitivity factor $k = k_0(1 - f_e)^{-1}$ (K/W m^{-2}) to the imposed forcing, which is fairly uniform at about $k = 0.8$ K/W m^{-2} from low to middle latitudes, rising sharply to a sensitivity of $k = 3$ K/W m^{-2} over most of Antarctica and at the North Pole. The black dotted line for CO_2 again has a meaning different from the other (climate sensitivity) curves. Here, it represents the latitudinally dependent flux conversion factor k_0 relating ΔT_0 and ΔF_0.

While the above results may provide useful insight regarding the nature of climate feedback interactions and climate sensitivity, they should be viewed with caution because experimental validation of feedback sensitivity is a task that is very difficult to perform. Furthermore, while the feedback analysis is greatly facilitated by having

assumed that different feedback processes are effectively linear and independent, there is evidence that such is not entirely the case. In GCM simulations using two different sea-ice distributions, Hansen et al. (1984) showed that the snow/ice feedback efficiency can differ significantly (by about 30%), depending on control run sea-ice amount, and that this leads to an accompanying ~ 10% reduction in water vapor feedback efficiency and a ~ 20% increase in cloud feedback efficiency, even though the model's cloud physics and hydrological physics remained unchanged. Thus, there remains a continuing need for further analysis and modeling studies to identify and quantify the nonlinearities that may exist among different feedback interactions (see Roeckner et al., this volume).

While there is ample reason to believe that globally the averaged feedback sensitivity may be more robust than the zonal variation in feedback sensitivity, much remains to be done to instill greater confidence both in the magnitude of the feedback sensitivity and its latitudinal dependence. Also at issue is the degree of local climate response versus the degree of global response that will result from a locally imposed climate forcing perturbation.

In a recent study, Hansen, Lacis et al. (1993) performed a series of transient climate simulations covering the period 1850–2000. The simulations were similar in nature to the transient simulations described by Hansen et al. (1988) and included radiative forcing due to documented GHG increases, as well as hypothesized solar constant variability, reconstructed volcanic aerosol forcing, estimated anthropogenic aerosol increases (based on Charlson et al. 1992), and different values of climate model cloud feedback sensitivity. The results of this study showed that all of the above processes make important contributions to climate forcing, and that the model sensitivity that best fits the global surface temperature record over the past century is equivalent to 3 ± 1 K for doubled CO_2. This implies a globally averaged feedback efficiency factor of $f_e = 0.6$, with corresponding feedback magnification of $f_m = 2.5$.

CLIMATE RESPONSE

By climate response, we generally mean the transient adjustment of the climate system in response to the imposed radiative forcing. A good example of this is the change in stratospheric, tropospheric, and surface temperature in response to the Pinatubo volcanic eruption shown in Plate 2.7. In a broader sense, climate response also includes consideration of the regional and more localized temperature changes, as well as changes in other climate parameters such as precipitation, length of growing season, and the frequency and intensity of climate extremes, e.g., droughts and storms. Among the major concerns in our changing climate is that the frequency and severity of droughts over continental areas may increase with global warming (Rind et al. 1990). This could lead, for example, to a potentially positive feedback with respect to desert dust intensification.

Contemplating these problems brings us to an area of climate modeling that is not as well explored or understood as radiative forcing and feedback sensitivity. A better understanding of how to deal with natural climate variability is the key to being able to model and predict the local and regional climate response, which is of course the ultimate goal in climate modeling. The Pinatubo eruption again provides a good case in point. In their GCM simulations of the Pinatubo eruption, Hansen et al. (1992) showed global maps of temperature change for two identical model runs (except for slightly different initial conditions). While the globally averaged temperature changes were in close agreement between the two runs, large regional differences were observed, particularly over much of central and eastern Canada. By comparison, the observed surface temperature changes in the summer of 1992 were a factor 10 colder in eastern Canada than the predicted global mean temperature change. Meanwhile, temperatures in the western United States and western Europe were warmer than before the eruption, also reflecting the chaotic nature of climate variability. Until we gain a better understanding of natural variability, signatures of regional climate change will not be readily separable from climatic noise.

The statistical part of the climate noise problem can be addressed by performing multiple runs for a given climate experiment, using slightly altered starting conditions for model initialization and thus generating a statistical profile of the chaotic climate behavior. There are, however, two major areas where further model development is needed in order to improve the climate modeling performance:

1. a comprehensive ocean model with improved modeling capability of atmosphere/ocean interactions to permit more accurate climate response simulation over decadal time scales; and
2. an improved microphysical cloud model to enable simulation of the indirect forcing by exerted aerosols on cloud radiative properties, cloud diurnal cycle phase and amplitude, and cloud feedback efficiency.

DISCUSSION

We have shown that aerosol radiative properties are sensitive functions of particle size, optical depth, and composition, and that they exhibit strong variation with wavelength in both the solar and thermal regions of the spectrum. This can be used to advantage in remote-sensing applications to retrieve detailed aerosol information (if the appropriate measurements are made), or it can lead to large uncertainties in estimating aerosol radiative forcing if we lack the full information regarding aerosol size, composition, or optical depth.

Much detailed information has been accumulated mostly from ground-based observations to characterize the basic aerosol compositional types, their characteristic particle sizes, and typical optical depths, including their basic geographic distribution and seasonal variability. However, the available information does not have adequate

global coverage or sufficient quantitative detail to serve directly as an input aerosol climatology usable in climate modeling applications. Nor is it yet possible to separate unambiguously the natural and anthropogenic components of atmospheric aerosols, or to reconstruct fully the historical trend in aerosol buildup based on the history of fossil-fuel and biomass burning. These tasks remain as the principal goals of a combined observational and modeling effort to develop a comprehensive aerosol climatology that would (a) permit accurate documentation of the current radiative forcing of climate due to aerosols, (b) establish how the magnitude of this aerosol contribution may have increased in the past with growing industrialization, and (c) determine how this increase in anthropogenic aerosols may have masked the global warming due to GHG increases. The desire to document the change in radiative forcing due to changes in aerosol loading implies the need for global monitoring of aerosols and of aerosol radiative properties, a capability that currently does not exist. Only satellite-mounted instruments can yield truly global observations.

Currently available satellite instrumentation lacks the required calibration and measurement precision and does not have the necessary spectral coverage, to measure aerosol properties with accuracy that is sufficient to determine the impact of tropospheric and, in particular, anthropogenic aerosols on climate. Still, current satellite measurements, particularly AVHRR data, have provided valuable information on the geographical and time-dependent changes in tropospheric and stratospheric aerosols (e.g., Stowe et al. 1992); they have identified regions of desert dust incursions over oceans, detected regions of biomass burning, and measured plumes of industrial pollution and sulfate aerosols that are transported over ocean areas from continental source regions (see Kaufman, this volume). However, the one major limitation of these measurements is that they basically rely on single-channel detection and thus cannot provide information on aerosol size, shape, or composition. Also, the absolute calibration of AVHRR measurements is essentially a normalization that assumes the Earth's global albedo to be invariant and is therefore not adequate for long-term and interannual monitoring of aerosol change.

What is needed to improve the information content and monitoring capability of aerosol remote-sensing measurements is a more powerful measurement technique. The instrument of choice would be a precision photopolarimeter, prototypes of which have been flown on planetary missions, but have never flown in Earth orbit. The principal advantage of polarimetric measurement is that polarization is a relative measurement, and therefore capable of achieving measurement precision at the 0.1% level in degree of linear polarization, a level of precision that is needed to make full use of the subtle variations in polarization degree to infer aerosol radiative properties. As described earlier, polarimetric measurements (plus adequate spectral and phase angle coverage) can be used to infer particle size and optical depth, as well as particle shape and refractive index information with far more precision than is possible with measurements that rely on intensity only.

In any case, tropospheric aerosols are a difficult target for remote-sensing measurements, so a broad range of instruments is needed to take advantage of different

aerosol radiative characteristics. For example, the strong spectral features in extinction efficiency, shown in Plate 2.1 for desert dust at thermal wavelengths, and their strong dependence on particle size should be easily detectable in high resolution thermal spectra taken with a Fourier transform interferometer. In similar fashion, Pollack et al. (1991) were able to infer the particle size and optical depth of the El Chichon volcanic aerosol from extinction measurements that were made in the thermal window region of the spectrum. These measurements are important since they directly address the greenhouse contribution of the stratospheric aerosol rather than rely on what amounts to an extrapolation from particle size determinations made at visible wavelengths by remote-sensing techniques or by direct particle counting, both subject to uncertainties related to accurate determination of the large particle tail of the size distribution.

Changes in desert dust may have had important impact on climate in the past, but there are a number of uncertainties involved. Since desert dust tends to be fairly absorbing, measurement of the particle size distribution, on which the absorption is strongly dependent, is a crucial parameter to be measured. However, the composition of desert dust is geographically variable, so it is also important to make measurements of the single-scattering albedo in order to obtain some degree of closure on the radiative properties of desert aerosol. Modeling calculations indicate that, for global average conditions, values of single-scattering albedo less than approximately $\omega_0 = 0.85$ will tend to warm the climate while values greater than 0.85 will cool (Hansen et al. 1980). However, even though the aerosol may be neutral in its effect on the planetary energy balance, this does not mean that its effect on climate is negligible. Absorbing aerosols redistribute solar energy deposition by increasing atmospheric heating and decreasing solar energy absorption at the ground surface, thus affecting atmospheric stability and thereby impacting clouds and atmospheric circulation.

Compared to tropospheric aerosols, the climate impact of stratospheric aerosols is far better understood and measured. This is because instruments capable of making the necessary measurements were already in place when the Pinatubo eruption occurred. Together with ground-based and *in situ* measurements, it was possible to characterize the aerosol amount, particle size, composition, atmospheric distribution, including the time and spatial variability. It was then straightforward to calculate the radiative forcing and to perform climate model simulations. Obviously the problem of tropospheric aerosols is far more difficult since tropospheric aerosols come in many different varieties and are far more difficult to measure from satellite platforms. Nevertheless, the relative success in measuring and modeling the climatic effect of stratospheric aerosols serves as a useful role model to emulate in attempting to improve our understanding of tropospheric aerosols and their role in climate change.

Another problem area that complicates determination of the climatic impact of tropospheric aerosols is properly accounting for the indirect aerosol effect, particularly that of the anthropogenic component, on cloud radiative properties. The observed decrease in the diurnal amplitude of surface temperature (Karl et al. 1993) and its apparent association with cloud cover changes over continental areas (Hansen et al. 1995), point to the pressing need of not only having to measure changes in aerosol

amounts, compositions, and distributions, but also of having to monitor changes in cloud cover and in cloud radiative properties.

Many of these problems were addressed at a workshop on Long-Term Monitoring of Global Climate, held at the Goddard Institute for Space Studies in 1992. The workshop set out to determine what type of measurements and measurement accuracies were needed to measure and monitor the key climate variables in order to document adequately the changes in climate that are currently taking place. The basic conclusions summarized in the conference report (Hansen, Rossow et al. 1993) show that the currently available satellite instrumentation is not adequate for this task. What is needed to perform the required measurements is a set of well-calibrated satellite and *in situ* instruments with a long-term monitoring capability with the ability to measure changes in stratospheric and tropospheric aerosol amounts and their radiative properties, changes in atmospheric water vapor and temperature distributions, and changes in cloud cover and cloud radiative properties.

ACKNOWLEDGMENTS

This work was supported by the Department of Energy Interagency Agreement under the Atmospheric Radiation Measurement Program, and in part by the NASA Office of Mission to Planet Earth. We thank the Dahlem Workshop reviewers for their careful reviews of this manuscript and, especially, we thank R. Charlson and J. Heintzenberg for their helpful comments and suggestions. Finally, we want to thank N. Zakharova of Hughes STX for assistance with graphics.

REFERENCES

Andreae, M.O. 1995. Climatic effects of changing atmospheric aerosol levels. In: World Survey of Climatology, vol. 16, Future Climates of the World, ed. A. Henderson-Sellers. Amsterdam: Elsevier, in press.

Charlson, R.J., S.E. Schwartz, J.M. Hales, R.D. Cess, J.A. Coakley, Jr., J.E. Hansen, and D.J. Hofmann. 1992. Climate forcing by anthropogenic aerosols. *Science* **255:**423–430.

d'Almeida, G.A. 1987. On the variability of desert aerosol radiative characteristics. *J. Geophys. Res.* **92:**3017–3026.

Deshler, T., D.J. Hofmann, B.J. Johnson, and W.R. Rozier. 1992. Balloonborne measurements of the Pinatubo aerosol size distribution and volatility at Laramie, Wyoming during the summer of 1991. *Geophys. Res. Lett.* **19:**199–202.

Hänel, G. 1976. The properties of atmospheric aerosol particles as functions of the relative humidity at thermodynamic equilibrium with the surrounding most air. *Adv. Geophys.* **19:**73–188.

Hansen, J., I. Fung, A. Lacis, S. Lebedeff, D. Rind, R. Ruedy, and G. Russell. 1988. Global climate changes forecast by the GISS 3–D model. *J. Geophys. Res.* **93:**9341–9364.

Hansen, J.E., and A.A. Lacis. 1990. Sun and dust versus greenhouse gases: An assessment of their relative roles in global climate change. *Nature* **346:**713–719.

Hansen, J.E., A.A. Lacis, P. Lee, and W.C. Wang. 1980. Climatic effects of atmospheric aerosols. *Ann. NY Acad. Sci.* **338:**575–587.

Hansen, J.E., A.A. Lacis, D. Rind, G. Russell, P. Stone, I. Fung, R. Ruedy, and J. Lerner. 1984. Climate sensitivity: Analysis of feedback mechanisms. In: Climate Processes and Climate Sensitivity, ed. J. Hansen and T. Takahashi. Geophysical Monograph. *AGU* **29:**130–163.

Hansen, J., A. Lacis, R. Ruedy, and M. Sato. 1992. Potential climate impact of Mount Pinatubo eruption. *Geophys. Res. Lett.* **19:**215–218.

Hansen, J., A. Lacis, R. Ruedy, M. Sato, and H. Wilson. 1993. How sensitive is the world's climate? *Natl. Geog. Res. Explor.* **9:**143–158.

Hansen, J., W. Rossow, and I. Fung. 1993. Long-Term Monitoring of Global Climate Forcing and Feedbacks. NASA CP 3234. Proceedings of workshop held at Goddard Institute for Space Studies, New York, February 2–4, 1992, 91 pp.

Hansen, J., G. Russell, D. Rind, P. Stone, A. Lacis, S. Lebedeff, R. Ruedy, and L. Travis 1983. Efficient three-dimensional global models for climate studies: Models I and II. *Mon. Weather Rev.* **111:**609–662.

Hansen, J., M. Sato, and R. Ruedy. 1995. Long-term changes of the diurnal temperature cycle: Implications about mechanisms of global climate change. *Atmos. Res.*, in press.

Hansen, J.E., and L.D. Travis. 1974. Light scattering in planetary atmospheres. *Space Sci. Rev.* **16:**527–610.

Hofmann, D.J., and J.M. Rosen. 1983. Sulfuric acid droplet formation and growth in the stratosphere after the 1982 eruption of El Chichon. *Science* **222:**325–327.

IPCC (Intergovernmental Panel on Climate Change). 1990. Climate Change: The IPCC Scientific Assessment, ed. J.T. Houghton, G.J. Jenkins, and J.J. Ephraums. Cambridge: Cambridge Univ. Press.

Karl, T.R., P.D. Jones, R.W. Knight, G. Kukla, N. Plummer, V. Razovayev, K.P. Gallo, J. Lindseay, R.J. Charlson, and T.C. Peterson. 1993. A new perspective on recent global warming. *Bull. Am. Meteorol. Soc.* **74:**1007–1023.

Kiehl, J.T., and B.P. Briegleb. 1993. The relative roles of sulfate aerosols and greenhouse gases. *Science* **260:**311–314.

King, M.D., and Harshvardhan. 1986. Comparative accuracy of selected multiple scattering approximations. *J. Atmos. Sci.* **43:**784–801.

Koepke, P., and M. Hess. 1988. Scattering functions of tropospheric aerosols: The effects of nonspherical particles. *Appl. Opt.* **27:**2422–2430.

Labitzke, K., and M.P. McCormick. 1992. Stratospheric temperature increases due to Pinatubo aerosols. *Geophys. Res. Lett.* **19:**207–210.

Lacis, A.A., and J.E. Hansen. 1974. Parameterization for the absorption of solar radiation in the earth's atmosphere. *J. Atmos. Sci.* **31:**118–133.

Lacis, A., J. Hansen, and M. Sato. 1992. Climate forcing by stratospheric aerosols. *Geophys. Res. Lett.* **19:**1607–1610.

Lacis, A.A., and V. Oinas. 1991. A description of the correlated k–distribution method. *J. Geophys. Res.* **96:**9027–9064.

Lorenz, E.N. 1968. Climate determinism. *Meteorol. Monogr.* **30:**1–3.

McCormick, M.P., and R.E. Veiga. 1992. SAGE II measurements of early Pinatubo aerosols. *Geophys. Res. Lett.* **19:**155–158.

Minnis, P., E.F. Harrison, L.L. Stowe, G.G. Gibson, F.M. Denn, D.R. Doelling, and W.L. Smith, Jr. 1993. Radiative climate forcing by the Mount Pinatubo eruption. *Science* **259:**1411–1415.

Mishchenko, M.I. 1993. Light scattering by size-shape distributions of randomly oriented axially symmetric particles of a size comparable to a wavelength. *Appl. Opt.* **32:**4652–4666.

Mishchenko, M.I., and L.D. Travis. 1994a. Light scattering by polydisperse, rotationally symmetric nonspherical particles: Linear polarization. *J. Quant. Spectros. Radiat. Trans.*, **51:**759–778.

Mishchenko, M.I., and L.D. Travis. 1994b. Light scattering by polydispersions of randomly oriented spheroids with sizes comparable to wavelengths of observation. *Appl. Opt.* **33:**7206–7225.

Nakajima, T., M. Tanaka, M. Yamano, M. Shiobara, K. Arao, and Y. Nakanishi. 1989. Aerosol optical characteristics in the yellow sand events observed in May, 1982 at Nagasaki. Part 2. Model. *J. Meteorol. Soc. Japan* **67:**279–291.

Nilsson, B. 1979. Meteorological influence on aerosol extinction in the 0.2–40 μm wavelength range. *Appl. Opt.* **18:**3457–3473.

Palmer, K.F., and D. Williams. 1975. Optical constants of sulfuric acid. *Appl. Opt.* **14:**208–219.

Patterson, E.M., D.A. Gillete, and B.H. Stockton. 1977. Complex index of refraction between 300 and 700 nm for Saharan aerosols. *J. Geophys. Res.* **82:**3153–3160.

Penner, J.E., R.E. Dickinson, and C.A. O'Neill. 1992. Effects of aerosols from biomass burning on the global radiation budget. *Science* **256:**1432–1434.

Pollack, J.B., D. Rind, A.A. Lacis, J.E. Hansen, M. Sato, and R. Ruedy. 1993. GCM simulations of volcanic aerosol forcing. I. Climate changes induced by steady state perturbations. *J. Clim.* **6:**1719–1742.

Pollack, J.B., F.C. Witteborn, K. O'Brien, and B. Flynn. 1991. A determination of the infrared optical depth of the El Chichon volcanic cloud. *J. Geophys. Res.* **96:**3115–3122.

Prather, M. 1992. Catastrophic loss of stratospheric ozone in dense volcanic clouds. *J. Geophys. Res.* **97:**10,187–10,191.

Rind, D., R. Goldberg, J. Hansen, C. Rosenzweig, and R. Ruedy. 1990. Potential evapotranspiration and the likelihood of future drought. *J. Geophys. Res.* **95:**9983–10004.

Rind, D., and A. Lacis. 1993. The role of the stratosphere in climate change. *Surv. Geophys.* **14:**133–165.

Russell, P.B., J.M. Livingston, E.G. Dutton, R.F. Pueschel, J.A. Reagan, T.E. DeFoor, M.A. Box, D. Allen, P. Pilewskie, B.M. Herman, S.A. Kinne, and D.J. Hofmann. 1993. Pinatubo and pre-Pinatubo optical depth spectra: Mauna Loa measurements, comparisons, inferred particle size distribution, radiative effects, and relationships to lidar data. *J. Geophys. Res.* **98:**22,969–22,985.

Stowe, L.L, R.M. Carey, and P.P. Pellegrino. 1992. Monitoring the Mt. Pinatubo aerosol layer with NOAA/11 AVHRR data. *Geophys. Res. Lett.* **19:**159–162.

Tegen, I., and A.A. Lacis. 1994. GCM modeling of the climate impact of desert dust aerosols. In: 8th Conf. on Atmospheric Radiation, pp. 113–115. Nashville, TN: Am. Meteorological Soc.

Toon, O.B., J.B. Pollack, and B.N. Khare. 1976. The optical constants of several atmospheric aerosol species: Ammonium sulfate, aluminum oxide, and sodium chloride. *J. Geophys. Res.* **81:**5733–5748.

Toon, O.B., and R.P. Turco. 1991. Polar stratospheric clouds and ozone depletion. *Sci. Am.* **264:**68–74.

Twomey, S.A., M. Piepgrass, and T.L. Wolfe. 1984. An assessment of the impact of pollution on global cloud albedo. *Tellus* **36B:**356–366.

Volz, F.E. 1973. Infrared optical constants of ammonium sulfate, Sahara dust, volcanic pumice, and flyash. *Appl. Opt.* **12:**564–568.

WMO (World Meteorological Organization). 1983. Report of the Experts Meeting on Aerosols and Their Climatic Effects, ed. A. Deepak and H.E. Gerber. WCP–55. Geneva: WCP, 107 pp.

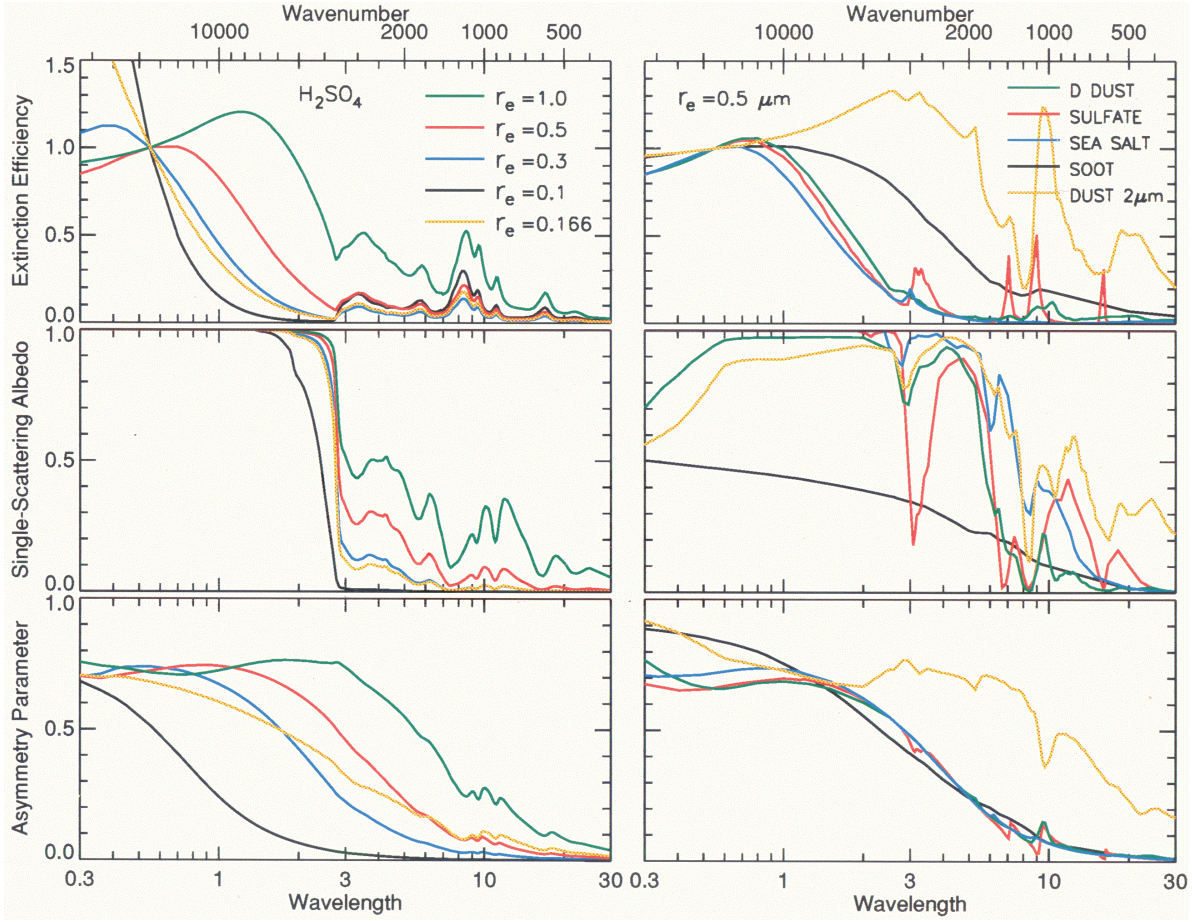

Plate 2.1 Mie-scattering calculated radiative parameters for H_2SO_4 (left) and representative tropospheric aerosols (right).

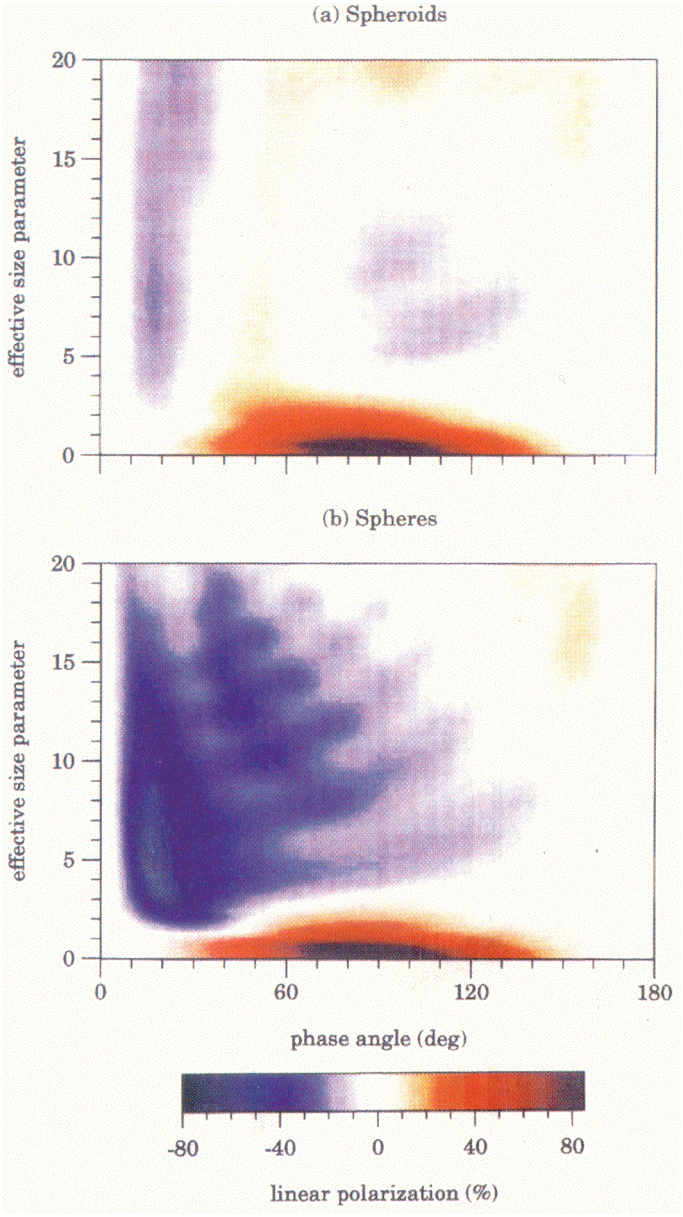

Plate 2.2 Degree of linear polarization as a function of phase angle and effective size parameter for polydispersions of volume-equivalent spheroids (Plate 2.2a) and spheres (Plate 2.2b).

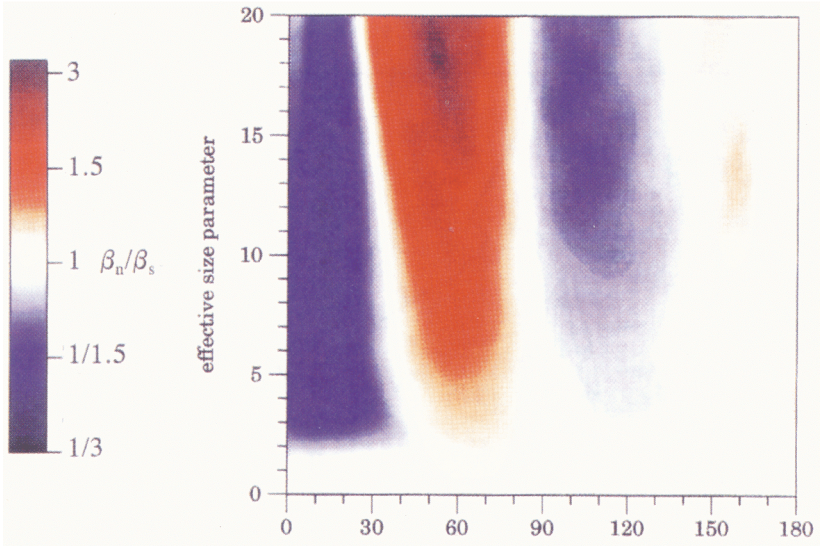

Plate 2.3 Ratio of nonspherical/spherical phase functions as function of phase angle for polydispersions of volume-equivalent spheroids and spheres shown in Plate 2.2.

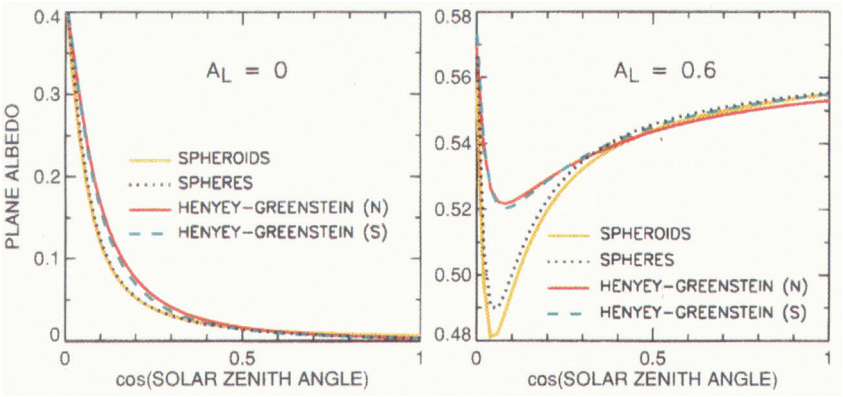

Plate 2.4 Plane albedo for polydisperse, randomly oriented spheroidal aerosols and volume-equivalent spherical particles. The index of refraction is $1.53 + 0.01i$, effective size parameter and effective variance are 20 and 0.2, respectively. The aspect ratio is 1.7 as measured by Nakajima et al. (1989). Results for Henyey-Greenstein phase functions using asymmetry parameters and single-scattering albedos of nonspherical and spherical aerosols are also shown.

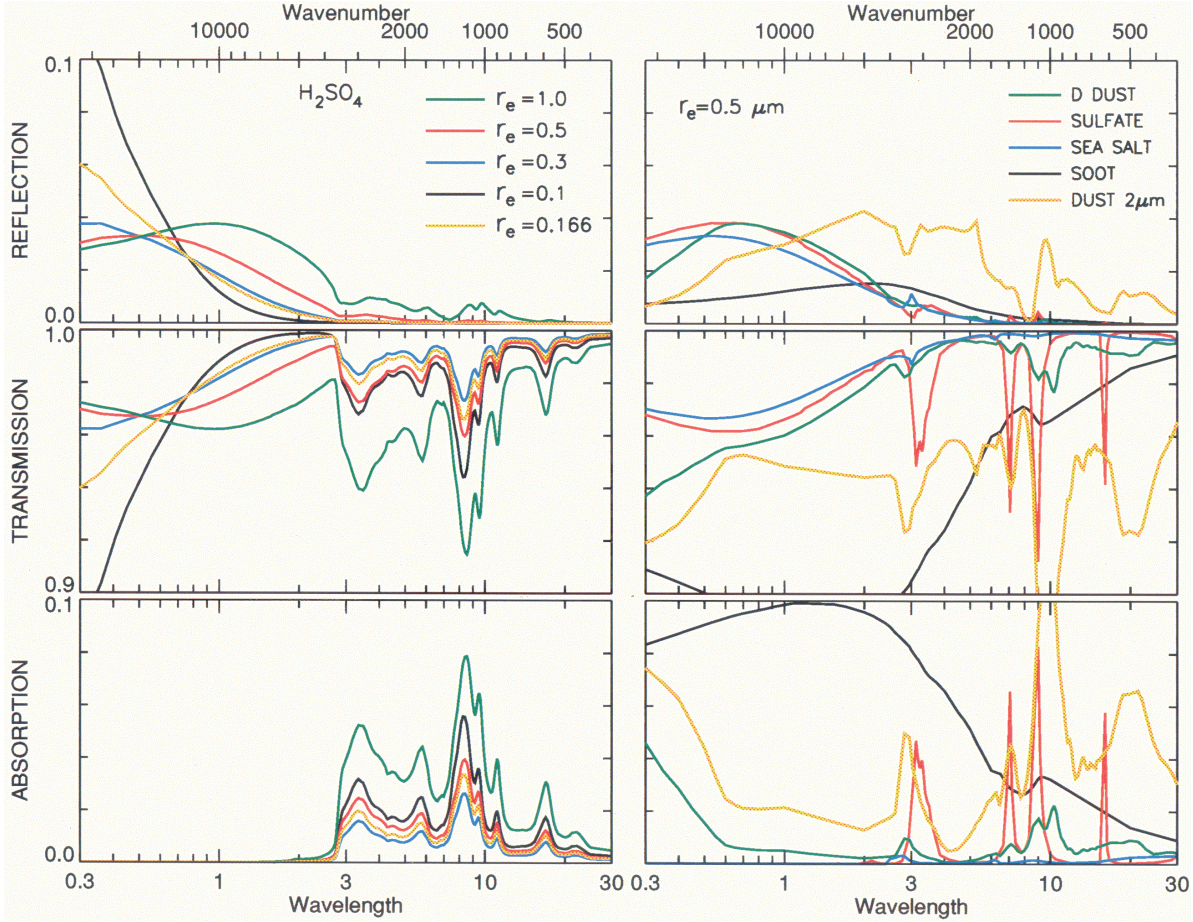

Plate 2.5 Globally integrated radiative properties for H_2SO_4 (left) and representative tropospheric aerosols (right) calculated for $\delta = 0.1$.

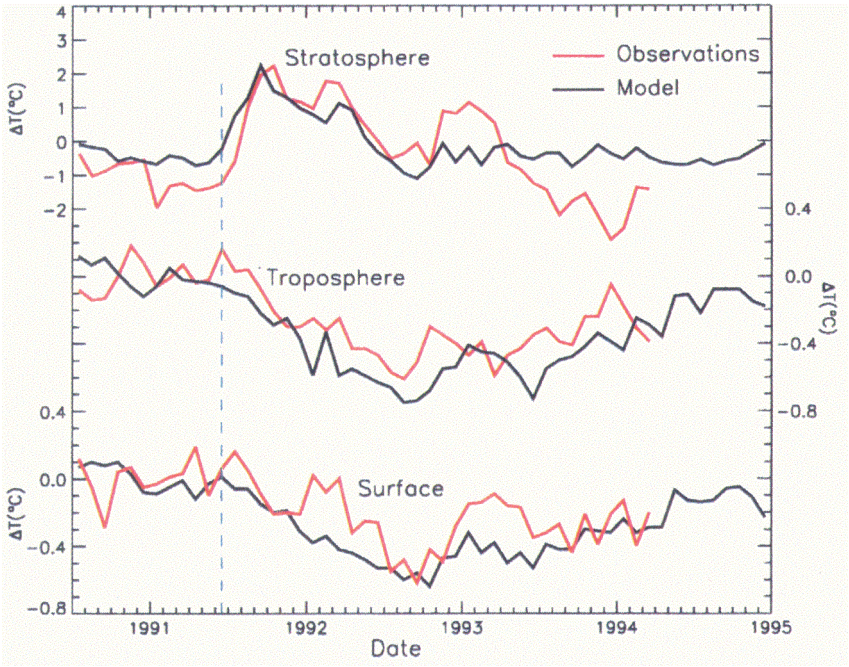

Plate 2.6 The observed and modeled changes in monthly stratospheric, tropospheric, and surface temperatures. Stratospheric observations are the 30-mb zonal mean temperatures at 10°S. Model results are for the 10 to 70 mb layer at 8°S to 16°S. Other results are essentially global. The Pinatubo eruption occurred on June 15, 1991. (Updated after Hansen, Lacis et al. 1993).

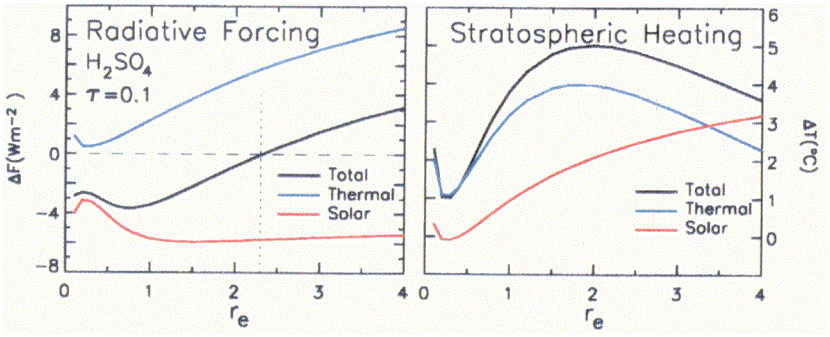

Plate 2.7 Radiative forcing at TOA by stratospheric H_2SO_4 aerosol with optical depth $\delta = 0.1$ as a function of effective radius (left), with corresponding stratospheric heating (right). The dotted line at $r_e = 2.2$ μm delineates particle size ranges that cool and warm the climate.

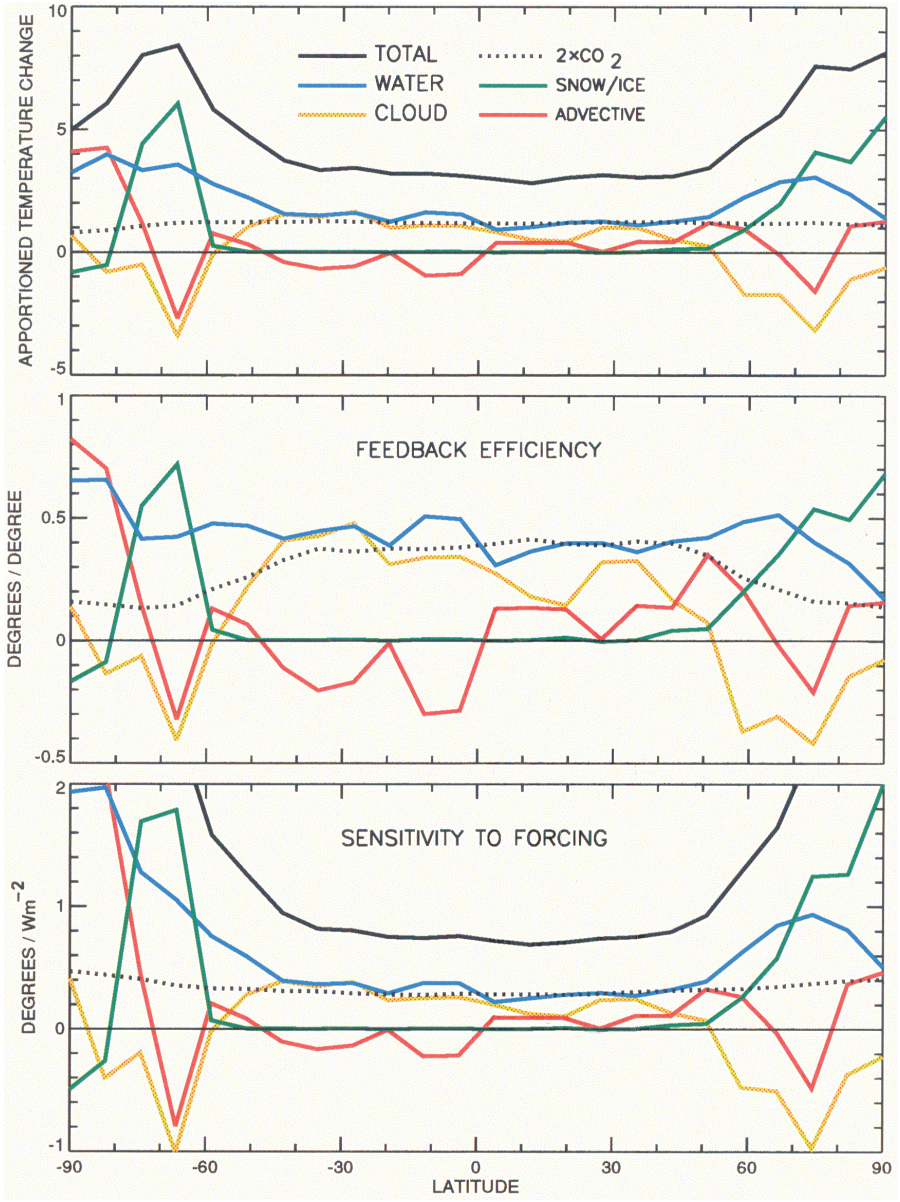

Plate 2.8 Apportioned temperature change, feedback efficiency, and sensitivity to radiative forcing in a doubled CO_2 GCM experiment. Blue, yellow, green, and red curves refer to contributions associated with changes in water vapor, clouds, snow/ice, and advective feedbacks. Solid black depicts total zonal annual mean (ZAM) temperature and feedback sensitivity changes. Black dotted line depicts direct CO_2 ZAM temperature changes and flux conversion factors.